Drivers of Climate-Model Biases in Antarctic Circumpolar Current Strength

---

Bachelor Thesis

B. Sc. Physics of the Earth System:
Meteorology, Geophysics, Oceanography

Christian-Albrechts-Universität zu Kiel
GEOMAR Helmholtz Center for Ocean Research

Author: Jakob Deutloff

Matriculation Number: 1125157

First Examiner: Prof. Dr. Joakim Kjellsson

Second Examiner: Dr. Torge Martin

July 2020

I. Zusammenfassung

In dieser Studie werden die Klimamodelle FOCI und zwei Versionen von HadGEM3 mit niedriger und mittlerer Auflösung, welche als LL und MM bezeichnet werden, bezüglich Fehlern in der Stärke des Antarktischen Zirkumpolarstroms (AZ) verglichen. Die horizontalen Auflösungen der jeweiligen Ozeanmodelle reichen von 1° in LL über 1/2° in FOCI bis zu 1/4° in MM.

Als mittlerer Transport des AZ durch die Drake Passage werden für LL 150 Sv, was mit aktuellen Messungen übereinstimmt, und deutlich niedrigere Werte von 78 Sv und 80 Sv für FOCI und MM festgestellt. Der Drake Passage Transport hängt direkt mit der horizontalen Struktur des AZ zusammen. Während in LL ein breiter, ostwärts fließender Strom gefunden wird, variiert der AZ horizontal deutlich stärker in FOCI und MM. Der zu niedrige Transport durch die Drake Passage in FOCI und MM wird durch zu niedrige Strömungsgeschwindigkeiten südlich von 58°S verursacht, welche teilweise durch starke ostwärtige Randströme, die entlang der Südspitze Südamerikas fließen, ausgeglichen werden. In der Mitte der Drake Passage und entlang ihres südlichen Randes verlaufen westwärts gerichtete Gegenströme in FOCI und MM, welche nicht mit aktuellen Messungen übereinstimmen. Diese Gegenströme sind mit zonalen Geschwindigkeiten von bis zu -23 $\mathrm{cm\,s^{-1}}$ in MM deutlich stärker ausgeprägt als in FOCI mit minimalen zonalen Geschwindigkeiten von -7 $\mathrm{cm\,s^{-1}}$.

Mit der thermischen Windgleichung werden zonale Geschwindigkeiten berechnet, wodurch der meridionale Dichtegradient als ein wichtiger Treiber des AZ identifiziert wird, welcher die beobachteten Unterschiede zwischen den Modellen in der Stärke des AZ teilweise erklärt. Der meridionale Dichtegradient verursacht ungefähr 50% des kompletten Transports der Modelle durch die Drake Passage, sowie Geschwindigkeiten, welche in ihrer Struktur den Modellgeschwindigkeiten gleichen. Die thermische Windgleichung wird ebenfalls auf das zonale Mittel der Dichte angewendet, was AZ Transporte und Geschwindigkeiten vergleichbar mit denen in der Drake Passage ergibt, mit Gegenströmen in FOCI und MM südlich von 63°S. Daher werden zu geringe Dichten südlich von 63°S als Ursache für einen zu schwachen AZ in FOCI und MM angenommen. Diese Dichteanomalien scheinen mit niedrigeren Salinitäten rund um die Antarktis zusammenzuhängen, wie im Vergleich mit LL sichtbar wird. Um die unterschiedlichen Salinitäten zu erklären, werden die Frischwasser Flüsse der Modelle südlich von 63°S verglichen. In MM werden stärkere Frischwasser Flüsse in den Ozean gefunden als in LL, was eine mögliche Erklärung für die verschiedenen Salinitäten der beiden Modelle liefert. Als weitere mögliche Ursache für die verschiedenen Verläufe der Isopyknen werden die Modelle auf Tiefenkovektion untersucht. Es wird Tiefenkonvektion in der Weddell See nachgewiesen, welche in FOCI wiederholt, in MM vereinzelt und in LL nie auftritt.

II. Abstract

In this thesis, we explore the Antarctic Circumpolar Current (ACC) strength biases in the FOCI climate model and the low- and medium-resolution versions of HadGEM3, known as LL and MM respectively. The three models form a resolution hierarchy of horizontal resolutions for their respective ocean components; 1° for LL, 1/2° for FOCI and 1/4° for MM.

We find that LL, with a mean Drake Passage transport of 150 Sv, is the only model within current observational estimates of the Drake Passage transport. The FOCI and the MM model have significantly lower mean Drake Passage transports of 78 Sv and 80 Sv respectively. The biases in FOCI and MM are found to be directly linked to a more complex horizontal structure of the ACC in the Drake Passage, with too low velocities south of 58°S, partly compensated by strong eastward boundary currents flowing around the tip of South America. In contrary, LL has a broad and homogeneous eastward flowing ACC in the DP. Both MM and FOCI feature westward countercurrents near the southern margin and in the middle of the Drake Passage, which are inconsistent with current observations. The westward countercurrents are stronger in MM than in FOCI, with zonal velocities down to -23 $\mathrm{cm\,s^{-1}}$ and -7$\mathrm{cm\,s^{-1}}$ respectively.

By calculating zonal velocities from the thermal wind balance the meridional density gradient is identified as a leading order driver of the ACC which explains part of the ACC strength biases in MM and FOCI. The Drake Passage transports driven by the meridional density gradient are found to be approx. 50% of the total Drake Passage transport. We show that the meridional density gradient drives velocity structures similar to those simulated by the respective models. We repeat the computation of zonal velocities for the zonal mean density fields, which yields similar transports and velocity patterns as in the Drake Passage, with countercurrents in FOCI and MM south of 63°S. The ACC strength biases in both FOCI and MM are therefore considered to be linked to a negative density bias south of 63°S.

We find that this density bias is in turn connected to a fresher upper ocean of FOCI and MM in the same region. In an attempt to explain this salinity bias, we compare the different freshwater fluxes of the models. For MM, higher downward freshwater fluxes are found to explain part of the models' negative salinity bias compared to LL. As another possible reason for the different density fields, deep convection is investigated. Persistent and sporadic deep convection in the Weddell Sea is found in FOCI and MM respectively, while no deep convection is observed in LL.

III Table of Contents

1. Introduction

1.1. Motivation

The Southern Ocean (SO), defined as the broad ocean region surrounding Antarctica (*Talley et al.*, 2011), hosts the most intensive current system in the world oceans, the Antarctic Circumpolar Current (ACC) (*Olbers et al.*, 2012). Its existence is due to the unique geography of the region, lacking zonal boundaries in the latitude band of the Drake Passage (DP). The DP is the narrowest meridional restriction of the SO, found between the southernmost tip of Chile and the Antarctic Peninsula. The ACC connects all the ocean basins and thereby permits a global, meridional overturning circulation (MOC) to exist (*Rintoul et al.*, 2001). The MOC, in turn, acts to transport heat and freshwater globally, connecting the ocean interior with the atmosphere-ocean boundary layer. Hence, it supports the exchange of gases like oxygen and carbon dioxide between the atmosphere and the ocean interior (*Meijers*, 2014). Therefore, a realistic representation of the ACC in climate models is vital for building confidence in model projections of future climate (*Beadling et al.*, 2019).

This study explores the ACC in the FOCI climate model (*Matthes et al.*, 2020) as well as the low- and medium-resolution versions of HadGEM3 (*Roberts et al.*, 2019), known as LL and MM respectively. The three models form a hierarchy of horizontal resolutions of their respective ocean components; 1° for LL, 1/2° for FOCI and 1/4° for MM. Even though *Watterson et al.* (2014) confirmed the link between better skill and finer horizontal resolution for climate models, the ACC transport through the DP is closer to observational estimates for the LL (1°, 155 Sv) than for the MM (0.25°, 90 Sv) HadGEM3 simulations (*Roberts et al.*, 2019). Several recent studies have compared these two models, also with regard to the ACC (*Menary et al.*, 2018; *Kuhlbrodt et al.*, 2018; *Roberts et al.*, 2019; *Jonathan et al.*, 2020). *Matthes et al.* (2020) stated that the DP transport in FOCI (1/2°, 83 Sv) is also weak. Possible reasons for too low DP transports in coupled climate models can be biases in the zonal wind stress, too low meridional density gradients in the DP latitude band, or poor representation of bathymetry (*Beadling et al.*, 2019). In the case of MM, low density gradients over the DP due to too low densities near the Antarctic shelf break, are suggested to play a major role in setting the ACC strength bias (*Menary et al.*, 2018; *Jonathan et al.*, 2020; *Kuhlbrodt et al.*, 2018). A possible mechanism that could set this density bias is deep convection in the Weddell Sea (*Menary et al.*, 2018).

This thesis aims to supplement the previous studies by introducing FOCI as a middle member to the resolution hierarchy. The main goals of this study are:

1. Calculate the DP transports of the models and compare them with the recent studies.

2. Investigate the ACC structure among the resolution hierarchy and how it is related to the DP transport.

3. Identify leading order mechanisms accounting for the model biases in ACC strength.

1.2. Dynamics of ACC and Overturning Circulation

This section provides a summary of the SO dynamics based on a conceptual model of the ACC and the MOC. Derivations of the Ekman dynamics and the thermal wind equations used in this model are given in the Appendix.

A simple explanation of the main dynamics driving the MOC and therefore also the ACC is given by *Vallis* (2006), using a conceptual, singe-hemisphere model with an idealized geometry of the SO. The dynamics of the model are kept as simple as possible with being Bousinesq (ρ is considered as constant ρ_0 in horizontal direction but varies in vertical direction $\rho(z)$ (*Gill*, 1982)) and planetary-geostrophic. A derivation of the planetary-geostrophic equations is given in *Olbers et al.* (2012). In contrast to the geostrophic equations, they include forcing by wind stress and buoyancy in the momentum equations. The buoyancy forcing of the model is imposed by fixing the surface buoyancy to two discrete values b_1 and b_2 at the southern and northern boundaries respectively, with a linear transition over the channel. The buoyancy is only determined by temperature since salinity is not taken into account. For the two different buoyancies, $b_2 > b_1$ holds. Wind stress forcing is exerted by purely zonal westerly winds, and is expressed as meridional Ekman velocity (v_E), leading to horizontal Ekman transport (M_E) and associated Ekman pumping/suction (w_E) given by the following equations:

$$\vec{f} \times \vec{M_E} = \vec{\tau_{\text{wind}}} \tag{1}$$

$$w_E = \nabla_h \cdot \vec{M_E}, \tag{2}$$

where $\vec{f} = (0, 0, f)$ is the Coriolis parameter and $\vec{\tau_{\text{wind}}}$ the wind stress. Equation 1 indicates that M_E is northward for eastward wind stress and $f < 0$. This northward Ekman transport peaks over the channel and decays to zero at the northern and southern edges of the basin. Following Eq. 2, w_E is therefore positive south of the channel and negative to the north of it. While the water is transported north, it warms up and its buoyancy increases up to b_2. A cyclonic subtropic qyre is located north of the channel while an anticyclonic subpolar gyre is located south of the channel, both of which can be explained by Sverdrup dynamics. In the region of the channel, however, zonal pressure gradients cannot exist, due to the lack of meridional land barriers (*Vallis*, 2006; *Meredith et al.*, 2011). Nevertheless, to comply

with mass balance, a poleward return flow over the channel must exist to make up for the northward Ekman transport. This return flow is found just under the sill as zonal pressure gradients may be supported by the bathymetry. Any deeper below the sill, the basin is filled with water of buoyancy b_1. Therefore, the warm and light water from the north must lie above it. Since warm water of buoyancy b_2 is flowing southwards under the sill, the regime becomes convectionally unstable and the buoyancy is made equal to the surface buoyancy over the whole channel watercoloumn down to the sill. The isopycnals in this region are consequently vertical, and this meridional density gradient drives a strong zonal current, obeying the thermal wind equation,

$$\frac{\partial}{\partial z}\begin{pmatrix} u \\ v \end{pmatrix} = \frac{g}{\rho_0 f_0}\begin{pmatrix} \partial\rho/\partial y \\ -\partial\rho/\partial x \end{pmatrix}, \tag{3}$$

where u, v are zonal and meridional velocities respectively, g is gravity, ρ_0 is reference density and f_0 is Coriolis parameter (here assumed constant). Hence, a circumpolar channel with zonal wind forcing is characterised by a deep meridional overturning circulation together with a strong zonal current, even if diapycnal diffusivity goes to zero. If diapycnal diffusivity was non-zero, a second overturning cell would form. In this cell, cold and dense water is getting mixed with warm and light water under the sill which is then upwelled. This diffusive loss of dense water would be compensated by surface formation of new dense water south of the channel, leading to a deep, diffusively driven overturning circulation (*Vallis*, 2006).

Most of the circulation features introduced in the idealised model above can be linked to the observed circulation of the SO. The upper wind driven overturning cell is identified as the "Deacon Cell", consisting of northward Ekman transport at the surface and southward flowing deep water at depth supported by the bathymetry (*Meredith et al.*, 2011). The lower diffusivity driven overturning cell can be identified with the Antarctic Bottom Water (AABW) cell (*Vallis*, 2006). This two-cell structure was also found by *Lumpkin and Speer* (2007). Cyclonic subpolar gyres are located in the Weddell and Ross Seas with estimated transports of 30-50 Sv (*Rintoul et al.*, 2001) and 20 Sv (*Reid*, 1997) respectively. Cold and dense shelf waters are formed in both the Weddell and Ross Seas (*Talley et al.*, 2011) due to heat loss and brine rejection in coastal polynyas and under the ice shelves. The dense shelf water spills down the continental slope, where it entrains with Circumpolar Deep Water and forms AABW. The AABW spreads northward along the bathymetry into all three main ocean basins (*Orsi et al.*, 1999).

However, the real dynamics of the SO are of course much more complex than those of *Vallis* (2006) model. First, the density of seawater is not only a function of temperature, but of temperature, salinity and pressure (*Jackett and Mcdougall*, 1995). In addition, eddies

play an essential role in the ACC dynamics (*Tansley and Marshall*, 2001). The ACC in the conceptual model is highly baroclinically unstable, due to the vertical isopycnals. If baroclinic eddies were allowed to form, mesoscale eddies would slump the isopycnals, and thereby reduce the ACC strength (*Vallis*, 2006). Furthermore, the barotropic component of the ACC is determined by the balance between bottom friction and wind stress. Using an idealised channel model, *Tansley and Marshall* (2001) showed that increasing the bottom friction by a factor five reduces the circumpolar transport by almost the same factor.

1.3. Drake Passage Transport

Measurements of the total DP transport remain a challenging task, mainly due to a lack of information about the strength and structure of the near bottom currents (*Donohue et al.*, 2016). A long time canonical DP transport estimate was provided by the International Southern Ocean Studies (ISOS) program, which took place from the late 1970s to the early 1980s. They suggested mean transport through the DP of 134 Sv (*Donohue et al.*, 2016). This value was taken as a benchmark for climate models for decades.

To estimate the transport related to the near bottom currents, two field campaigns with in-situ measurements, the DRAKE campaign and the cDRAKE campaign were set up in February 2006 and November 2007 respectively. The DRAKE campaign consisted of 10 subsurface current meter moorings and five full depth hydrographic sections taken by R/V Polarstern. As an early result of the DRAKE campaign, *Meredith et al.* (2011) proposed a mean transport of the ACC through the DP of (133 ± 7) Sv, which is not conflicting with the estimate of ISOS. This value is estimated from two highly resolved (20 km station spacing) Lowered Acoustic Doppler Current Profiler sections through the DP, sampled within three weeks.

A significantly higher value of (173.3 ± 10.7) Sv was found by *Donohue et al.* (2016) who analysed 21 current and pressure-recording inverted echo sounders (CPIES), spanning across the DP and 21 CPIES spanning 120 km cross- and 240 km downstream (*Meredith et al.*, 2011) from the cDRAKE campaign. The difference between older measurements is mainly caused by higher barotropic transports of (45.6 ± 8.9) Sv which have been determined by near bottom velocities measured with the CPIES (*Donohue et al.*, 2016).

1.4. Structure of the ACC

The property distribution of the ACC shows a predominantly zonal structure (*Talley et al.*, 2011) due to the open zonal passage in the DP latitude band. Several fronts can be charac-

terized by strongly northward tilted isopycnals over the whole watercoloumn, which makes them the regions with the highest velocities of the ACC.

Orsi et al. (1995) identified three major fronts in the DP by evaluating all hydrographic data of the SO that was available at this point of time. They named the fronts from north to south the Subantarctic Front (SAF), the Polar Front (PF) and the Southern Front which is also referred to as the Southern ACC Front (SACCF). These fronts are not strictly zonal, since they are directly impacted by the bottom topography (*Orsi et al.*, 1995).

Firing et al. (2011) investigated the vertical structure of the ACC in the DP, using direct velocity observations of shipboard acoustic Doppler current profiler (SADCP) data, taken over four and a half years by the R/V Laurence M. Gould. They also took into account the Southern Ocean State Estimate (SOSE), a 1/6° eddy permitting general circulation model which is fit to observational data (*Mazloff et al.*, 2010). Depth sections over the DP down to 1000 m of the absolute velocity of the SADCP and SOSE data were analysed. They show the three cores of the ACC in the DP, associated with the three mean observed fronts from north to south, the SAF, PF and SACCF, which have higher velocities than $20\,\mathrm{cm\,s^{-1}}$. Between those cores, the velocity is significantly lower (Fig. 3 in *Firing et al.* (2011)). The three fronts have a significant influence on the transport of the ACC. The transport in the upper 1042 m peaks at the locations of the fronts, while it has minimums between the fronts with transports around zero (Fig. 4 in *Firing et al.* (2011)).

2. Data and Methods

2.1. Data

2.1.1. FOCI

The Flexible Ocean and Climate Infrastructure version 1 (FOCI) is a coupled earth system model recently introduced by *Matthes et al.* (2020) and is the successor of the Kiel Climate Model. The configuration of FOCI is given in Tab. 1.

The NEMO ocean model uses the tripolar ORCA05 grid. From the southern limitation of the grid at 77°S to 20°N, the gridlines follow a geographical Mercator grid and deviate further north, forming two north poles. The z-axis is discretized by 46 z-levels, varying from 6 m at the surface to 250 m in the deep ocean. Since the ORCA05 grid is not fine enough to resolve mesoscale eddies, FOCI uses *Gent and Mcwilliams* (1990) eddy parameterisation (*Treguier et al.*, 1997). The ECHAM atmosphere model uses a N48 Gaussian grid with 95 vertical hybrid sigma-pressure levels.

Air-sea fluxes performed by the OASIS-MCT coupler are calculated in the atmospheric part of the model, which limits their resolution to the one of the atmosphere model.

In this study, the last 100 years of the 1500-year pre-industrial control run under 1850 climate conditions (FOCI-piCtl) are used.

2.1.2. HadGEM3-GC3.1

The Hadley Centre Global Environment Model 3 - Global Coupled vn. 3.1 (HadGEM3-GC3.1) is a coupled earth system model as well, developed by the Met Office. We use the LL and the MM version of HadGEM3-GC3.1, described by *Roberts et al.* (2019). Both are designed for the Coupled Model Intercomparison Project phase 6 (CMIP6) HighResMIP, a new experimental design to investigate the link between climate model fidelity and horizontal resolution (*Haarsma et al.*, 2016). The configurations of both models are specified in Tab. 1.

The z-axis of the ORCA grids used in MM and LL differs from the one used in FOCI with being subdivided into 75 z^*-levels with 1m top level thickness. They are called z^*-levels since they are space and time dependent, following the variations of sea surface height. By ignoring this time and space dependency of the z*-levels, we introduce an error, which should, however, be small and not impact our main results. The atmosphere grids N96 and N216 are both regular latitude-longitude grids with 85 hybrid height levels. Like FOCI, LL

	LL	MM	FOCI
Atmosphere Component	GA7.1 (*Walters et al.*, 2019)	GA7.1	ECHAM6.3 (*Stevens et al.*, 2013)
Ocean Component	NEMO3.6 (*Madec et al.*, 2017)	NEMO3.6	NEMO3.6
Land Component	GL7.1 (*Walters et al.*, 2019)	GL7.1	JSBACH3 (*Brovkin et al.*, 2009)
Sea Ice Component	CICE5.1 (*Hunke et al.*, 2015)	CICE5.1	LIM2 (*Fichefet and Maqueda*, 1997)
Coupler	OASIS-MCT (*Valcke*, 2013)	OASIS-MCT	OASIS-MCT
Atmosphere Grid	N96 ($1.25° \times 1.875°$)	N216 ($0.56° \times 0.83°$)	N48 ($1.8° \times 1.8°$)
Ocean Grid	ORCA1 (1°) L75	ORCA025 (1/4°) L75	ORCA05 (1/2°) L46
Coupling freq.	1h	1h	3h
Eddy Parameterisation	Yes (*Treguier et al.*, 1997)	No	Yes (*Treguier et al.*, 1997)
Model Run	control-1950 (*Roberts et al.*, 2019)	control-1950 (*Roberts et al.*, 2019)	FOCI-piCtl (*Matthes et al.*, 2020)

Table 1: Configurations of the different models used in this study: Their components with references, grids, coupling frequency, eddy parameterisations and the respective runs we used.

uses *Gent and Mcwilliams* (1990) eddy parameterisation (*Treguier et al.*, 1997), while this parameterisation is deactivated in MM, since the ORCA025 grid resolves mesoscale eddies.

We use 100 years from the 1000- and 600-year control-1950 experiment for LL and MM respectively. The control-1950 experiment runs under 1950 climate conditions.

2.2. Methods

2.2.1. Climatologies

In this study, climatologies of the data are used, except for the mixed layer depth (MLD), for which the whole time series is considered. The climatologies are obtained by taking seasonal means for austral summer (December - February, DJF), autumn (March - Mai, MAM), winter (June-August, JJA) and spring (September-November, SON).

2.2.2. Sections Over Drake Passage

We use two sections across the DP along which zonal velocities, transports, temperatures and salinities are investigated (Fig. 1). Section one goes along 67°W, which makes the

calculation of perpendicular zonal transports possible. The exact coordinates of section one are given in Tab. 2. Since velocities and scalars are staggered on the C-grid used in NEMO, velocities and scalars, e.g. temperature, are taken at slightly different latitudes. We select the sections in the model coordinates that are closest to 67°W and at the same time closest together. We therefore choose 66.5°W (LL), 66.75°W (FOCI) and 66.5°W (MM) for scalars and 67°W (LL), 67°W (FOCI) and 67.125°W (MM) for velocities. In FOCI, the transports are stored at the same coordinates as velocities, whereas in MM and LL, they are stored at the same coordinates as scalars. The transports are therefore sampled at 66.5°W for all three models. Section two is chosen in the cDrake area along the most commonly sampled line of *Firing et al.* (2011) (see their Fig. 1), to make the results comparable. The exact coordinates of section two are also given in Tab. 2. Along section two, the closest data points are picked.

2.2.3. Density

The potential density is calculated from the practical salinities and the potential temperatures of the models, using the EOS-80 formulation (*Jackett and Mcdougall*, 1995). First, the in-situ temperature is calculated from the practical salinity, the potential temperature and the depth with a reference pressure of 10.1325 dbar. The in-situ temperature together with the practical salinity and the depth is then used to calculate the potential density. As the reference pressure, 10.1325 dbar is used again. In the next step, 1000 kgm^{-3} are subtracted from the potential density to compute the density anomaly σ. Calculating the density from time-mean fields rather than at each model time step leads to some errors since EOS-80 is not linear. However, these errors are small and should not impact our main results.

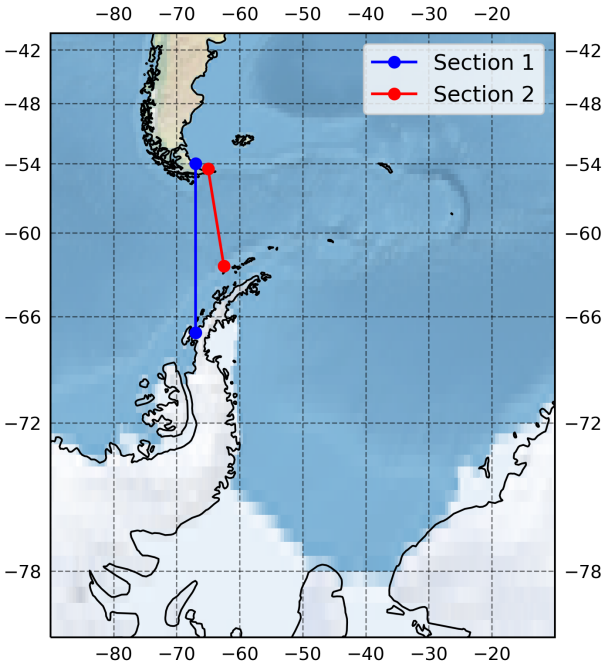

Figure 1: Section one at 67°W and section two along the most commonly sampled line of *Firing et al.* (2011) in the area of the cDrake array.

Section	Lat North / °S	Lon North / °W	Lat South / °S	Lon South /°W
1	54	67	67	67
2	54.5	65	62.5	62.5

Table 2: Coordinates of the sections over DP, with Lat North and Lon North as the latitudes and longitudes north of the DP, Lat South and Lon South as the latitudes and longitudes south of the DP.

2.2.4. Density Gradient and Thermal Wind

Based on σ, the meridional density gradient is calculated. For this purpose, the grid cell width is used as a finite difference. Since neither the grid cell width in °S ($\Delta\Phi$) nor the grid cell width in m (Δy) is given for MM and LL, it is computed from the latitudes:

$$\Delta\phi(j) = (\phi(j+1) - \phi(j-1)) \cdot 0.5,$$
$$\Delta y(j) = \Delta\phi(j) \cdot R_0 \cdot \frac{\pi}{180}.$$

Where ϕ is latitude in degrees, j the grid cell index along the y-axis and $R_0 = 6371 \cdot 10^3\,\mathrm{m}$ the earth radius. The density gradient is subsequently computed,

$$\frac{\Delta\sigma}{\Delta y}(k,j) = \frac{\sigma(k,j+1) - \sigma(k,j)}{\Delta y(j)},$$

with k being the index along the z-axis. The zonal velocity u is then estimated with Eq. 3. We use $u = 0\,\mathrm{m\,s^{-1}}$ as the boundary condition in the lowest layer to isolate the effect of the horizontal density gradient. The constant density ρ_0 is chosen as $1027.292\,\mathrm{kgm^{-3}}$ and f_0 as $f(60°S)$ with $-1.263 \cdot 10^{-4}\,\mathrm{s^{-1}}$.

2.2.5. Freshwater Fluxes

The zonal means normally include all longitudes. Only for the zonal-mean freshwater fluxes, the region of the DP is excluded, due to the large influence of Chile and the Antarctic Peninsula with strong precipitation on their western sides. In order to exclude those fluxes from the zonal mean, the longitude band from 50°W to 80°W is disregarded in the zonal mean. The LL and MM data-sets containing freshwater flux (FWF) from melting icebergs and river runoff are remapped from the ocean to the atmosphere grid, to make them compatible with the data-sets containing evaporation and precipitation, which are also on the atmosphere

grid. The sums of the freshwater fluxes F_{EPR} and F_{net} are:

$$F_{\mathrm{EPR}} = E - P - R,$$
$$F_{\mathrm{net}} = E - P - R - F_{\mathrm{ice}},$$

where E is evaporation, P precipitation, R runoff from rivers and icebergs and F_{ice} freezing and melting sea ice. Melting and freezing of sea ice is only included in F_{net}. From the LL and MM data only F_{EPR} was available. Therefore, a direct comparison between FOCI and the two HadGEM models regarding the FWF must be considered carefully.

In order to quantify the importance of the different freshwater fluxes, a simple estimation of the freshening caused by the different FWFes of the models south of 63°S is made, based on the considerations of *Kjellsson et al.* (2015). The temporal and spatial mean FWF in the latitude band between 77°S and 63°S is calculated for every model with the above mentioned restrictions for zonal means of the FWF. From those means, inter-model differences ΔFWF are formed. A mixed layer of $A = 1\,\mathrm{m}^2$ area and $H = -100\,\mathrm{m}$ depth is assumed. The initial values of salinity and density are $S_1 = 35$ PSU and $\rho_1 = 1030\,\mathrm{kg\,m^{-3}}$. The height Δz of the freshwatercolumn with density $\rho_0 = 1000\ \mathrm{kg\,m^{-3}}$ which results from ΔFWF applied for $T = 100$ years is calculated. The constant factor $C = 1 \cdot 10^{-3}\,\mathrm{m\,kg^{-1}}$ is used to obtain Δz in m

$$\Delta z = \Delta FWF \cdot A \cdot T \cdot C.$$

Next, Δz is added to the mixed layer watercoloumn which yields the new Salinity $S_2 = S_1 + \Delta S$ and the new density ρ_2. Combining the new watercolumns conservation of mass,

$$(H + \Delta z)\rho_2 = H\rho_1 + \Delta z\rho_0,$$

and the salt conservation,

$$(H + \Delta z)\rho_2(S_1 + \Delta S) = H\rho_1 S_1,$$

results in

$$\Delta S = -\frac{S_1 \Delta z \rho_0}{H\rho_1 + \Delta z\rho_0}.$$

2.2.6. Standard Deviation and Time Series of the Mixed-layer Depth

In order to visualise regions with seasonal deep convection, the standard deviation of the MLD is calculated. In MM and FOCI, the mean MLD of one area each is calculated and plotted as a time series. The respective coordinates are listed in Tab. 3.

Model	Latitudes / °S	Longitudes / °W
FOCI	64.23 - 67.30	12.25 - 47.25
MM	60.15 - 66.81	-0.50 - 34.50

Table 3: Coordinates of the regions the spatial mean MLD is calculated for.

3. Results

3.1. Velocities in Drake Passage

We start by comparing the zonal velocities on two cross sections, one at 67°W and one comparable to the cDRAKE line of *Firing et al.* (2011) (sections one and two of Fig. 1).

Each model exhibits similar velocity structures on both sections (Fig. 2) but there are significant differences between the models. The ACC is broad in LL with more pronounced latitudinal structure being in FOCI and MM (Fig 3).

On section two, LL shows a smooth velocity profile, with the highest velocities found near the surface at 57°S and near the northern shelf edge at 55.5°S (Fig. 2). The zonal velocity of LL does not exceed values of 31 cm s^{-1} with eastwards velocities over the whole profile

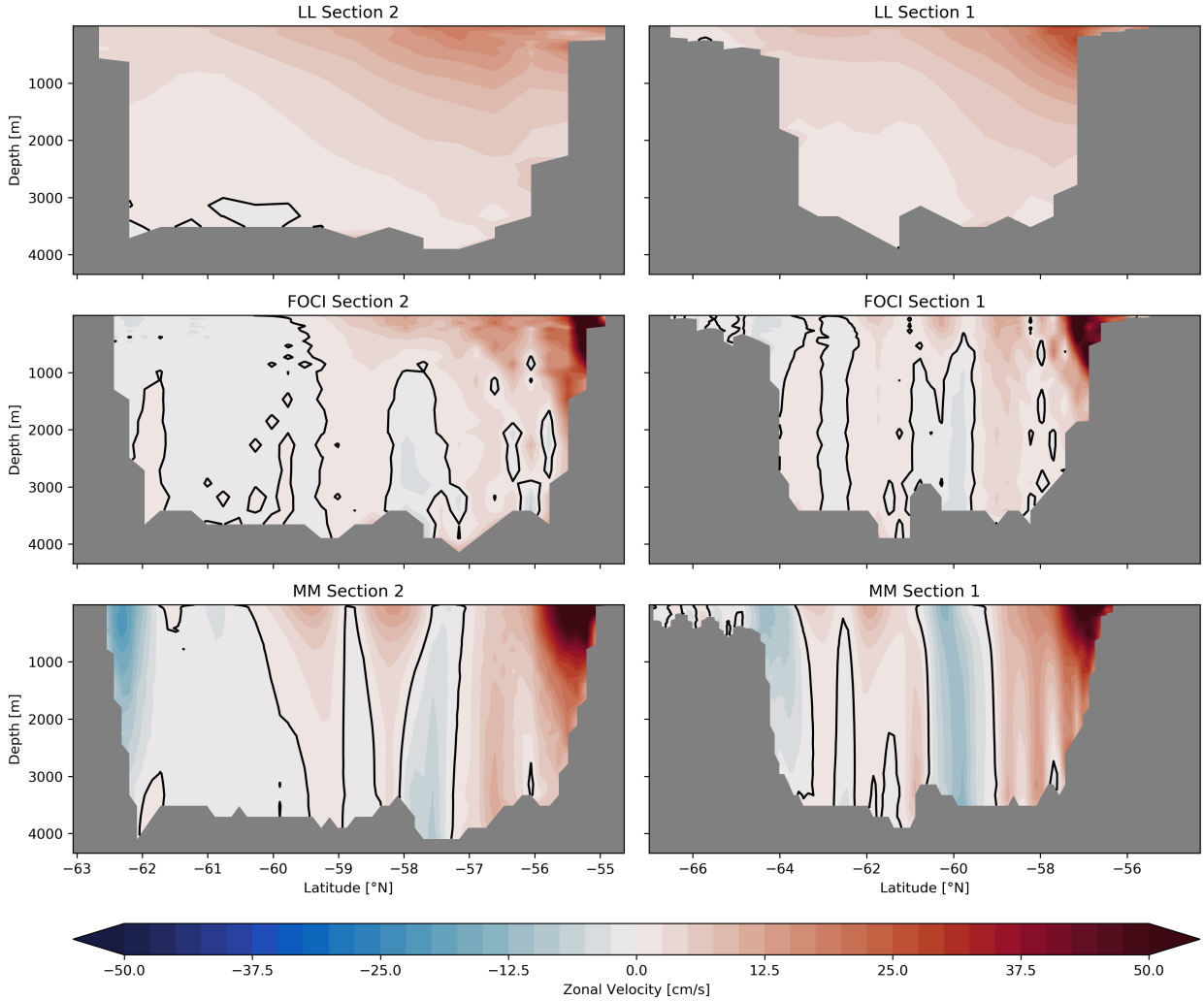

Figure 2: Time-mean zonal velocities on section one and section two (see Fig. 1). The black lines on each plot are the 0 cm s^{-1} contour.

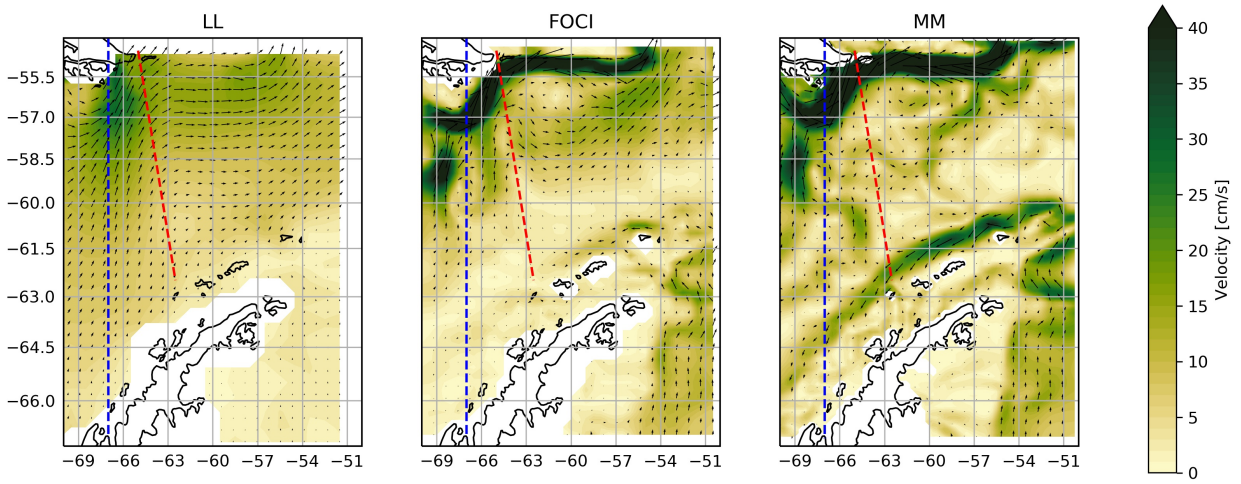

Figure 3: Time-mean depth averaged velocities of the top 1000 m. The blue and red dotted lines indicate the positions of section one and two respectively (see Fig. 1).

except, for a few very weak westward countercurrents near the seafloor in the south. The zonal velocity of FOCI on section two has weak countercurrents throughout the watercolumn from the southern boundary of the channel to 59.5°S and a second one in the middle of the DP around 58°S, reaching from the bottom up to 1000 m depth. The minimum zonal velocity in FOCI on section two is -7 $cm\,s^{-1}$. In contrary to LL, FOCI contains a strong eastward boundary current near the surface on the northern side of the DP with velocities up to 90 $cm\,s^{-1}$. This boundary current with comparable velocities is also found in MM on section two, but even wider and deeper. The rest of the zonal velocity structure in MM also resembles the one in FOCI. The main difference between the two models is that the countercurrents are even stronger in MM, particularly near the southern boundary, with a minimum velocity of -23 $cm\,s^{-1}$. In the middle of the DP, MM has two countercurrents, reaching over the whole watercoloumn.

The zonal velocity patterns on section one are very similar to those on section two (Fig. 2). This is consistent with average 1000 m velocities at the two sections (Fig. 3). The main differences are, that LL has even fewer countercurrents on section one, while the ones in FOCI and MM have slightly changed in position and strength. The countercurrents are less intense in the south, but therefore more pronounced in the middle of DP, especially in MM. This can be explained by examining the vertically averaged horizontal currents (Fig. 3). The countercurrents near the southern margin of the DP in FOCI and MM emerge from the Weddell Sea and are much more pronounced in MM. Their magnitude is decreasing while they flow westward along the shelf break. Therefore, their signal is weaker on section one. The strong countercurrent of MM in the middle of the DP on section one seems to be part of a meander that crosses section one at 62°S, turns west between section one and two and

flows back across section one at 60°S (cf. Fig. 2 and Fig. 3).

The strong northern boundary currents of FOCI and MM exist on both sections (Fig. 2). In FOCI, this boundary current is sharper than in MM, especially on section one, where the area of velocities over 20 cm s^{-1} is limited to a depth of approx. 1000 m. This is again in good agreement with the velocities of the top 1000 m. The eastward boundary currents with mean velocities in the top 1000 m over 40 cm s^{-1} in the north of the DP are a dominant feature of MM and FOCI, flowing around the southern tip of South America (Fig. 3).

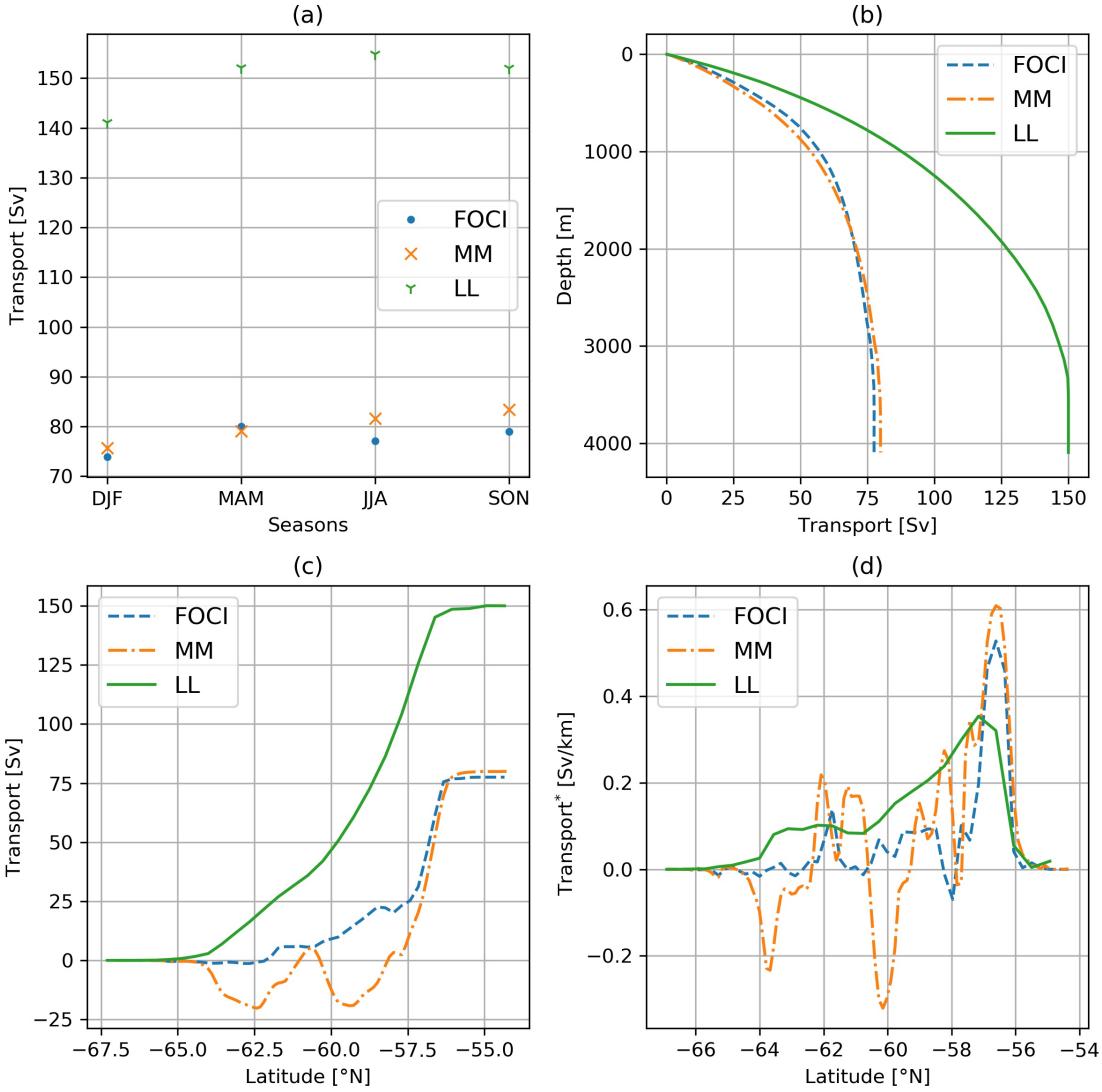

Figure 4: Transports across section one (see Fig 1). (a) The total transport for each season. (b) Cumulative sum along z of the temporal averaged and meridionally integrated transport. (c) Cumulative sum along the latitudes of the temporal averaged and vertically integrated transport. (d) Vertical sum of the temporal average transport, divided by the meridional grid cell width in km. Transport*: Transport per unit distance.

3.2. Drake Passage Transport

We now calculate the DP transport across section one for each season. We observe no pronounced seasonality of the DP transport in any of the three models (Fig. 4a). We find that time-averaged transports are 150 Sv, 78 Sv, and 80 Sv for LL, FOCI and MM respectively. To get an impression of the structure of the ACC and how it is related to its transport, vertical and meridional sums of the transports are calculated. The vertical cumulative sum of the meridional integrated time-average transport (Fig. 4b) is nearly equal for FOCI and MM, while LL has higher transports over the whole depth. Additionally, all three curves are very smooth. Therefore, the difference of the DP transports of LL, FOCI and MM seems not to be emerging from any particular depth level.

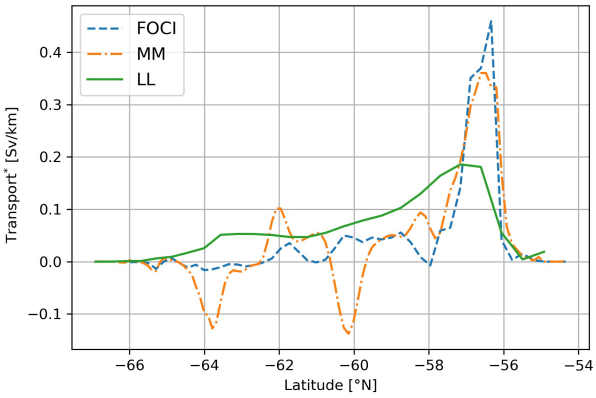

Figure 5: Vertical sum of the temporal average transport of the upper 1000 m divided by the grid cell width in km on section one (Fig. 1). Transport*: Transport per unit distance

In order to understand the impact of the latitudinal variations of the zonal velocities on the DP transport along section one, we calculate the vertically integrated time-averaged transport per km and also as a cumulative sum cross the DP (Fig. 4d and c). The cumulative sum along the latitudes is positive everywhere for LL. For FOCI it is around zero until 62°S with a minimum of -2.72 Sv. In MM, the westward transport is even stronger with two minimums of the cumulative sum in Fig. 4c, lower than -20 Sv at 62.5°S and 59.3°S. This gives a first hint towards the importance of countercurrents for the DP transport. The vertically integrated time-averaged transport per km further emphasises this. It has two strong negative peaks in MM at 63.7°S and 60.3°S, varies around zero in FOCI between 66°S and 62°S and is positive everywhere in LL. The locations of those negative peaks in MM match the locations of the countercurrents on section one (Fig. 2). The transport per km peaks towards the northern edge of the section for all three models and is highest for LL which makes its cumulative sum in Fig. 4c catch up with FOCI's towards the north. This displays the influence of the northern boundary currents on the DP transport in FOCI and MM which are partly compensating for the low transports south of 58°S.

The latitudinal variations of the DP transport are very similar if integrated over the full depth or only the upper 1000 m (compare Fig. 4d and Fig. 5). This indicates that the DP transport is strongly barotropic. We find that the transport per km in the upper 1000 m

in the region of the northern boundary currents around 56.5°S is stronger in FOCI than in MM. However, the full depth-integrated transport per km is stronger in MM than in FOCI at this latitude, i.e. the transport in FOCI is more surface intensified than in MM, which agrees with the zonal velocity patterns on section one (Fig. 2).

3.3. Zonal Winds

The zonal-mean zonal wind stress is investigated as a possible reason for the observed DP transport biases since it was found to impact the strength of the ACC in CMIP3 models (*Russell et al.*, 2006).

Due to the strong seasonality of the wind stress, all four seasons are taken into account. While MM and LL show rather similar patterns, the zonal wind stress maximum of FOCI is shifted to the north during MAM, JJA and SON (Fig. 6). This is a known bias in the ECHAM6 atmosphere model (see Fig. 13 and 14 of *Stevens et al.* (2013)). The position of the zonal wind stress maximum in LL and MM matches the annual mean maximum zonal wind stress of the ERA-Interim reanalysis from *Beadling et al.* (2019) during all seasons except for DJF. In DJF, the zonal wind stress looks nearly the same for all three models, with the maximum shifted towards the north compared to the ERA-Interim. In MAM, the maximum wind stress of LL ($0.188\,\mathrm{N\,m^{-2}}$) and FOCI ($0.192\,\mathrm{N\,m^{-2}}$) is slightly higher than the one of MM ($0.172\,\mathrm{N\,m^{-2}}$). Since zonal-mean zonal wind stress shows no pronounced inter-model variability, it is not considered to play a crucial role in setting the inter-model DP transport biases.

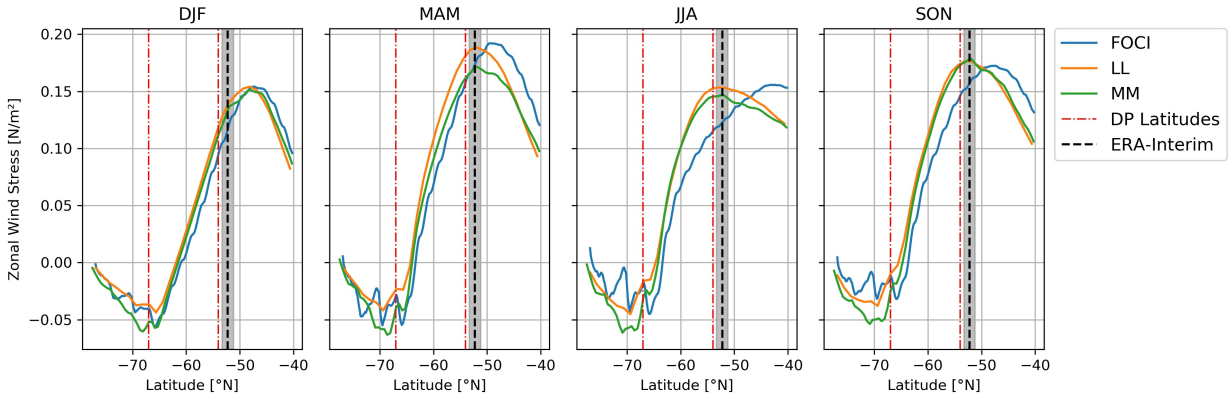

Figure 6: Zonal mean of the zonal wind stress for each season. Red dashed lines indicate the DP latitude band from section one (see Fig. 1). The black dashed line is the position of the annual mean maximum zonal wind stress from ERA-Interim reanalysis data with its error (grey shaded) from *Beadling et al.* (2019).

3.4. Influence of the Density Gradient on the ACC

Another possible cause of the ACC biases among the resolution hierarchy is the meridional density gradient. We quantify the contribution of DP transport from the meridional density gradient by calculating the volume transport using the thermal wind equation (Eq. 3). We apply this equation to both the density gradient across DP as well as the zonal mean.

The slopes of the isopycnals in the DP (middle row Fig. 7) lead to the meridional density gradient ($\partial\sigma/\partial y$) fields in the lowest row of Fig. 7. We find that $\partial\sigma/\partial y$ is negative nearly everywhere in LL, with the lowest values in the north. In contrary, FOCI and MM have positive values in the south and are strongly negative in the north of the DP, both exceeding $-2\cdot10^{-6}\,\mathrm{kg\,m^{-4}}$. Such low values are less frequent in LL, but they also occur on the northern shelf. While $\partial\sigma/\partial y > 0$ is only dominant south of 62° in FOCI, MM has $\partial\sigma/\partial y > 0$ also in the middle of the DP around 61°S. The largest positive meridional density gradients (above $5\cdot10^{-7}\,\mathrm{kg\,m^{-4}}$) are found in MM at the southern margin of the DP and around 60.5°S.

The vertical shear of the zonal thermal winds, calculated using the thermal wind balance (Eq. 3), is inversely proportional to the meridional density gradient. Therefore, the patterns of both quantities in Fig. 7 show some similarities. The zonal thermal winds of LL are positive nearly everywhere in the DP, while FOCI and MM have strong and narrow positive jets near the surface in the north and countercurrents in the south, which are stronger in MM (Fig. 7). The general zonal velocity structure obtained from the meridional density gradients is comparable with the zonal model velocities on section one (Fig. 2). However, the countercurrents in the middle of the domain cannot be fully explained by thermal wind balance. The countercurrent in MM around 60°S is shifted to the south by one degree and has a more baroclinic structure than in the model velocities, while FOCI's countercurrent at the same latitude is not displayed at all by the thermal winds (Fig. 7). The zonal transport calculated from the thermal winds in the DP is highest in LL with 69 Sv, lowest in MM with 36 Sv and FOCI lies between them with a value of 44 Sv. Comparing this with the model transports given in Section 3.2, the meridional density gradient explains 46%, 45% and 58% of the total DP transport of LL, MM and FOCI respectively.

The average σ of FOCI ($27.72\,\mathrm{kg\,m^{-3}}$) is lower than the one of MM ($27.79\,\mathrm{kg\,m^{-3}}$) or LL ($27.82\,\mathrm{kg\,m^{-3}}$) (cf. Fig. 8 middle row). The zonally and full-depth averaged potential density differences $\Delta\rho$ between 65°S and 45°S, used by *Beadling et al.* (2019) as a key measure for climate models ACC quality, are in reasonable agreement with the zonal-mean density patterns of the models. We find, that $\Delta\rho$ is slightly higher for LL with $0.18\,\mathrm{kg\,m^{-3}}$ than for MM and FOCI with $0.16\,\mathrm{kg\,m^{-3}}$ for both of them.

The zonal-mean meridional density gradient in the lower row of Fig. 8 displays the tilting

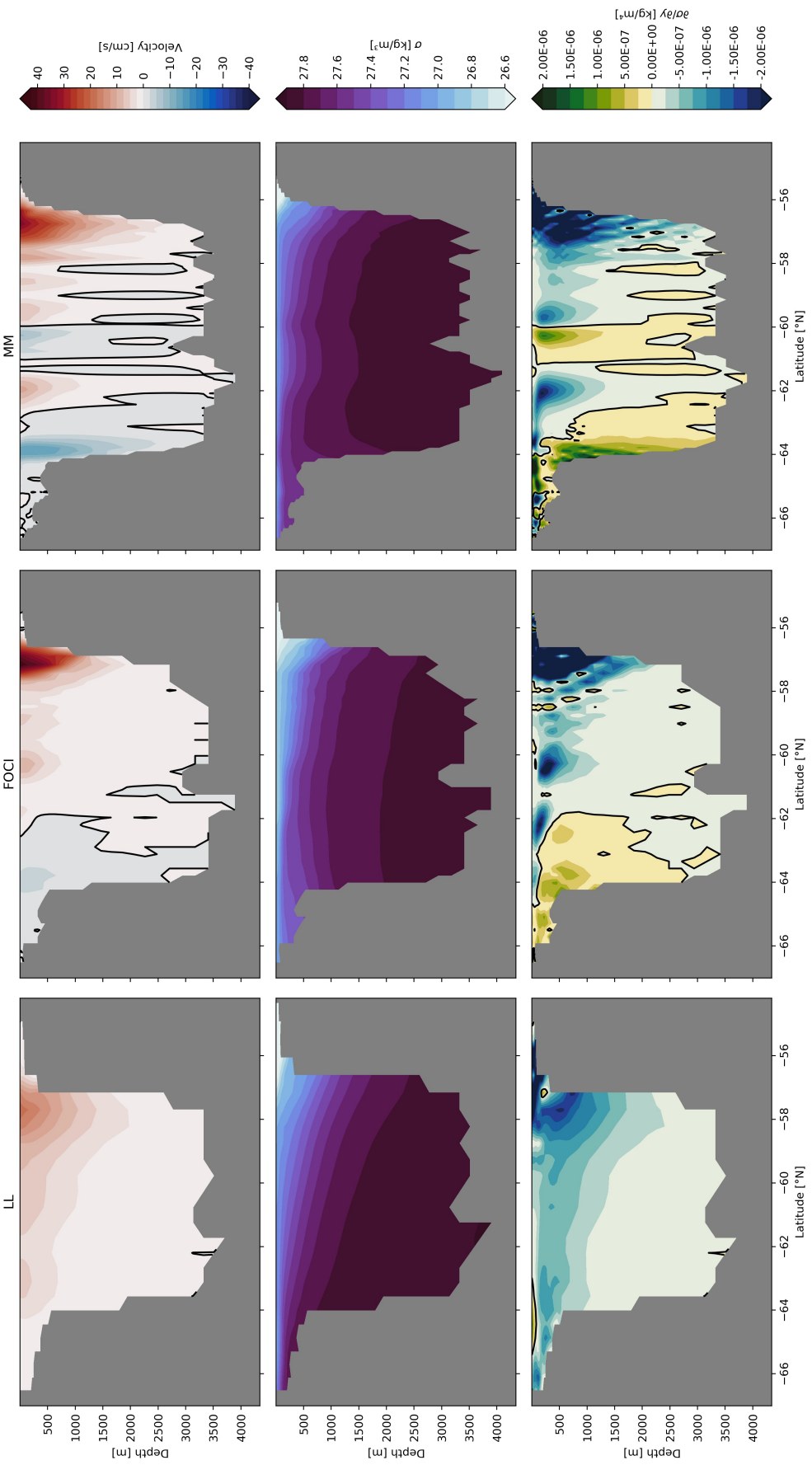

Figure 7: Temporal mean of the zonal velocities derived from the thermal wind balance (Eq. 3) (upper row), the potential density anomaly σ (middle row) and the meridional potential density gradient (lower row) on section one (see Fig. 1). Black lines are the zero contour line.

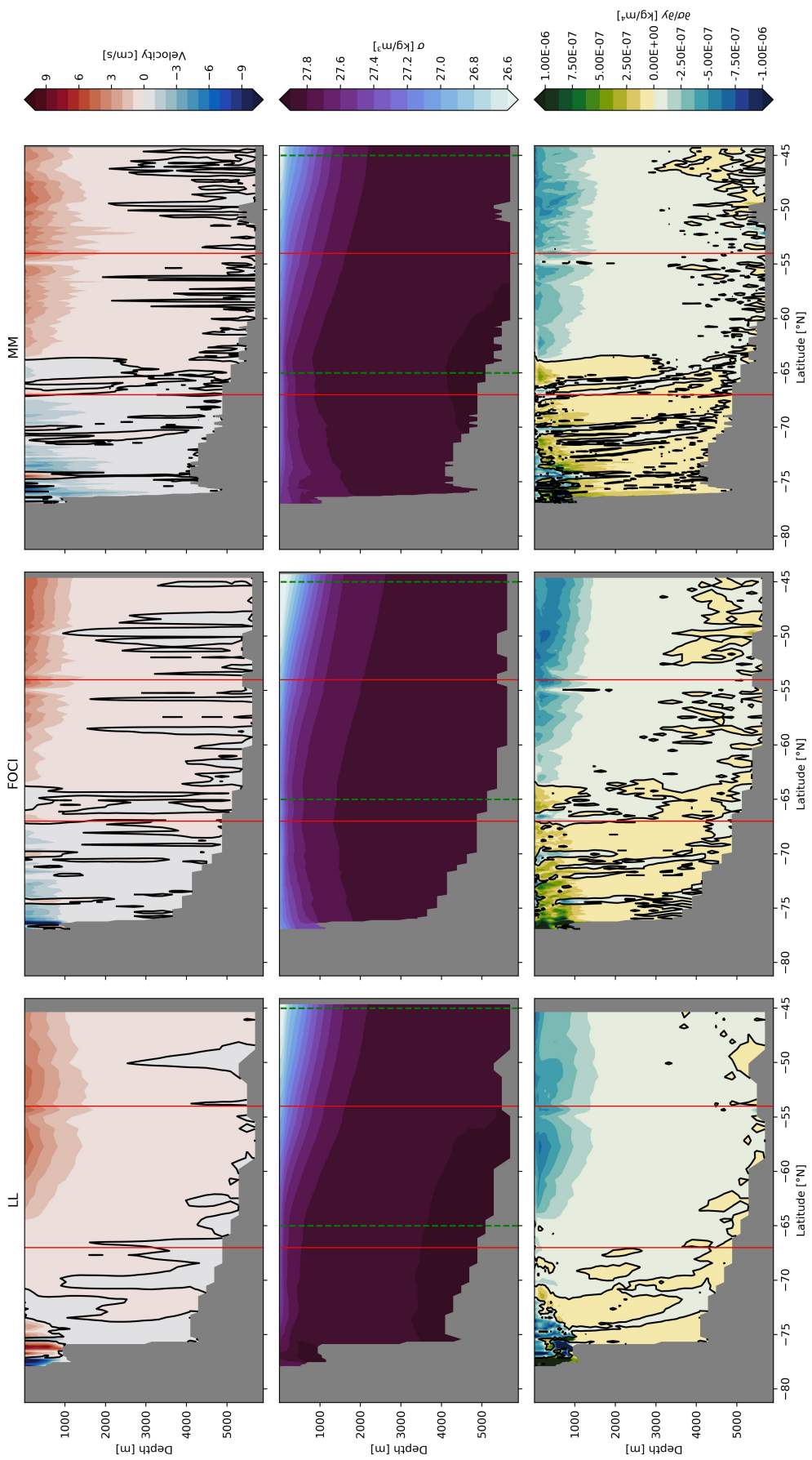

Figure 8: Zonal and temporal means of the zonal velocities derived from the thermal wind balance (Eq. 3) (upper row), the potential density anomaly σ (middle row) and the meridional potential density gradient (lower row). Red lines indicate the DP latitude band from section one (see Fig 1). Green dashed lines indicate the latitudes for the calculation of the meridional density gradient as in *Beadling et al.* (2019). Black lines are the zero contour line.

of the zonal-mean isopycnals (middle row of Fig. 8). From the southern margin of the SO to 63°S, $\partial\sigma/\partial y > 0$ holds nearly everywhere in MM and FOCI with values higher than $3.75 \cdot 10^{-7}\,\mathrm{kg\,m^{-4}}$ in several areas of the top 1000 m. North of 63°S, $\partial\sigma/\partial y < 0$ holds for the whole watercolumn except for some areas near the bottom in MM and FOCI. The minimum and maximum values of the zonal-mean $\partial\sigma/\partial y$ are found in the upper 1000 m in all three models. In contrary to FOCI and MM, the zonal-mean $\partial\sigma/\partial y$ of LL is positive merely south of the DP latitudes and reaches values higher than $3.75 \cdot 10^{-7}\,\mathrm{kg\,m^{-4}}$ only at the southern margin of the channel.

The zonal velocity estimated from the thermal wind balance depicts countercurrents extending from the southern margin of the SO into the DP latitudes up to 63°S in MM and FOCI, while countercurrents are found mainly south of the DP latitudes in LL. North of 63°S, positive thermal winds are found with their maximum at the surface in all three models. Like the zonal mean meridional density gradient, the zonal thermal winds are only less than half as strong as in the DP (compare Fig. 7 and Fig. 8).

The zonal transport in the DP latitude band calculated from the zonal-mean thermal winds is highest for LL with 79 Sv, lowest for FOCI with 40 Sv and MM lies between them with 49 Sv.

3.5. Salinity and Potential Temperature in Drake Passage and as Zonal Means

Around half of the DP transport and much of the differences in structure of the zonal velocities between LL, FOCI and MM can be explained by thermal wind balance. We therefore examine what sets the meridional density gradients in all three model simulations. The salinity and potential temperature along section one and the zonal means are compared between the models (Fig. 9 and 10).

We find, that FOCI and MM are fresher and colder than LL south of 64°S in the DP (Fig. 9). The isopycnals align better with the salinity field than with the potential temperature in the DP in all three models, suggesting density is more sensitive to salinity than temperature at these latitudes. In MM, salinity and potential temperature are getting lower towards the southern shelf break, which is not observed in FOCI.

Near the northern margin of the DP, sharp horizontal temperature gradients with a temperature maximum on the northern shelf in FOCI and MM are found, while the transition to higher values in the north is more smooth in LL. The salinity fields on the northern side of the DP depict lower $\partial S/\partial y$ in FOCI and MM compared to LL near the South American

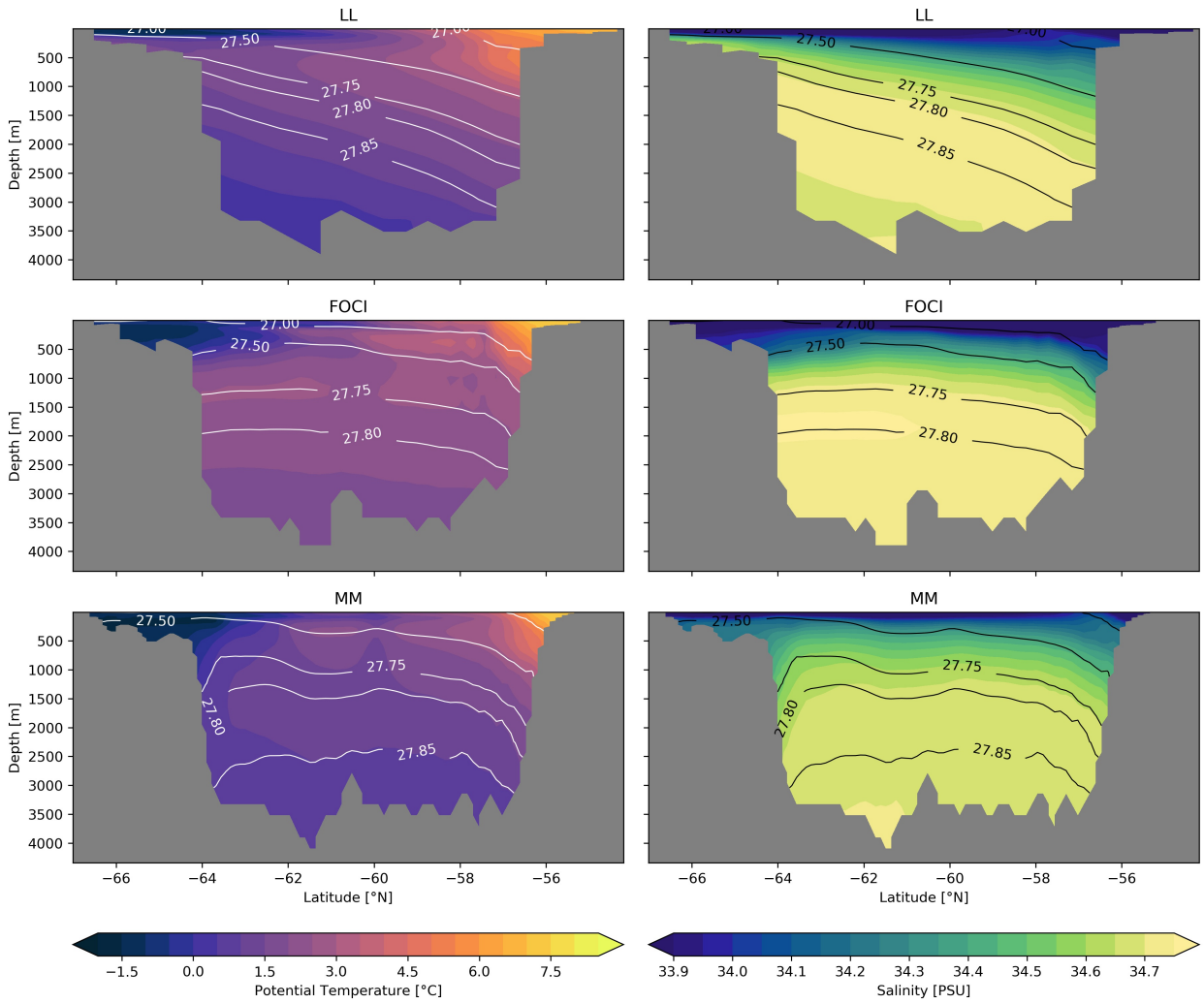

Figure 9: Time mean potential temperature and salinity on section one (see Fig 1) with σ contour lines.

shelf break (Fig. 9). In the DP, the FOCI model is warmer below 1000 m and fresher in the upper 500 m compared to MM and LL.

The signal of a cold and fresh water mass near the surface at the southern margin of the SO is also visible in the temporal and zonal mean salinity and potential temperature fields of FOCI and MM (Fig. 10). In the upper 1000 m south of 63°S FOCI and MM are fresher than LL. For the salinity $\partial S/\partial y > 0$ holds nearly everywhere in the upper 1500 m from 63°S to the southern margin of the SO in FOCI and MM, while $\partial S/\partial y < 0$ is predominant in this region in LL. The isopycnals are again well aligned with the isohalines, indicating the strong influence of the salinity on the density. The zonal means of salinity and potential temperature show that FOCI is fresher near the surface and warmer at depth compared to MM and LL, which is in good agreement with FOCI being the model with the least dense SO. Even though there are only a few isothermals below 1000 m, temperature differences in

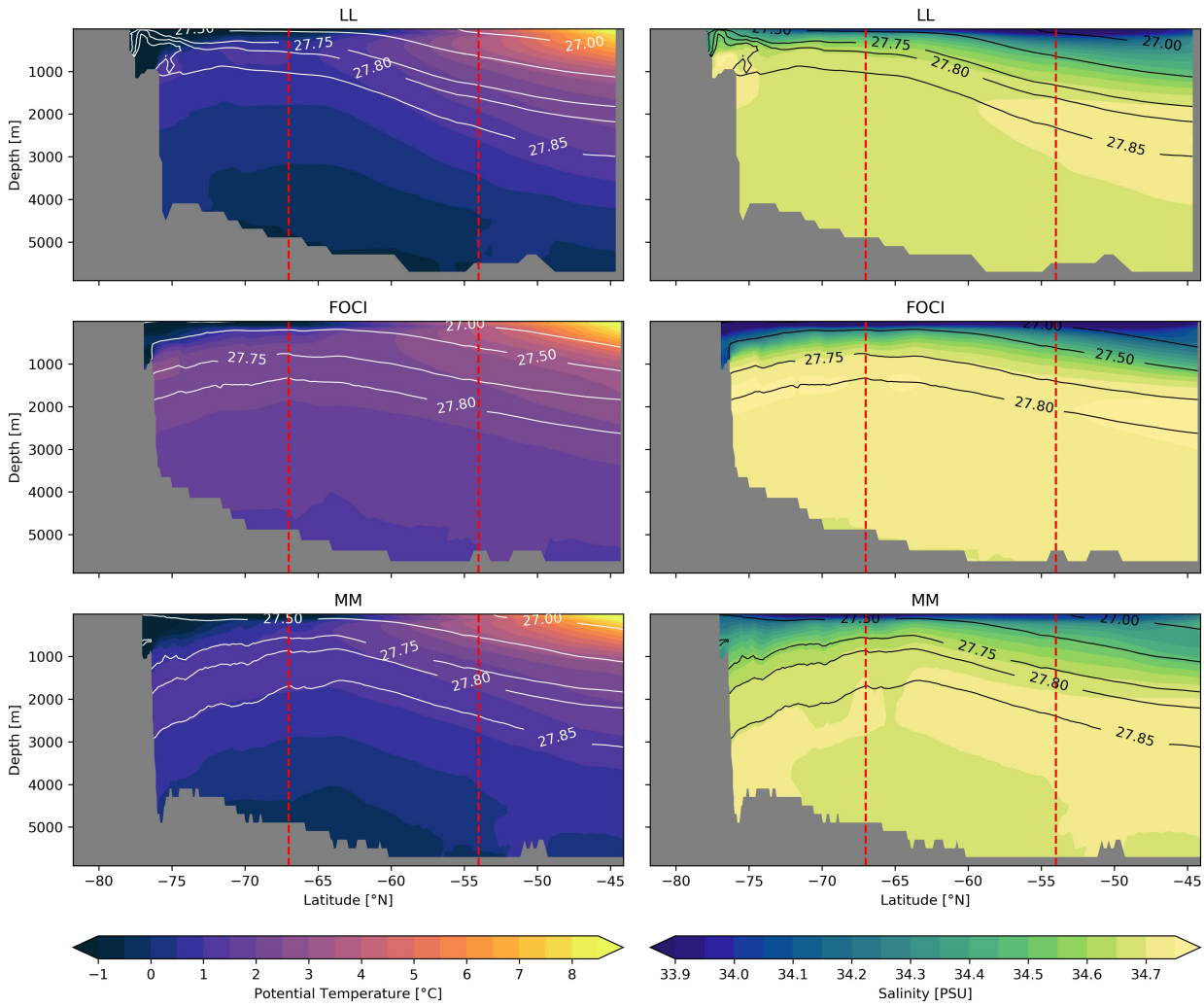

Figure 10: Temporal and zonal mean of potential temperature and salinity with σ contour lines. The red dashed lines indicate the DP latitude band from section one (see Fig. 1).

this region between the models can be observed. Compared to LL, the warm bias of FOCI increases towards south, and MM also has higher temperatures than LL from 55°S to the southern margin of the SO (Fig. 10). This is accompanied by different $\partial T/\partial y$. South of 63°S and 65°S $\partial T/\partial y < 0$ is dominant below 1000 m in MM and FOCI respectively. In LL this slumping of the isothermals sets in further south at 72°S.

In both the DP and the zonal mean one reason for $\partial\sigma/\partial y > 0$ in FOCI and MM at high latitudes, driving the countercurrents (see Sec. 3.4) seems to be the low salinity near the surface in the respective regions. The low potential temperatures also found there would only cause the water to be more dense. Below 1500 m, warmer temperatures in FOCI and MM compared to LL towards Antarctica seem to be a key driver of the zonal mean $\partial\sigma/\partial y > 0$, since the salinity is nearly homogeneous at these depths in all three models (Fig. 10). The eastward boundary currents around the southernmost tip of South America are probably

Model	FWF/kg m^{-2} s^{-1} $\cdot 10^{-5}$	ΔFWF/kg m^{-2} s^{-1} $\cdot 10^{-7}$	Δz/m	ΔS/PSU
LL	1.284			
FOCI	0.845	-43.82	13.82	5.423
MM	1.341	5.748	-1.813	-0.605

Table 4: Mean downward freshwater fluxes (FWF) between 77°S and 63°S from F_{net} of FOCI and F_{EPR} of MM and LL. The mean FWF differences between FOCI and LL or MM and LL (ΔFWF) together with the freshwatercolumn (Δz) caused by ΔFWF applied over 100 years and the respective changes in salinity (ΔS).

linked to the sharp temperature maximum on the shelf of South America and the lower $\partial S/\partial y$ towards the South American shelf break in FOCI and MM compared to LL.

3.6. Freshwater Fluxes and Deep Convection

In order to understand the differences in meridional density gradient across DP and in the zonal mean between the model simulations, we now turn to the freshwater budget. Comparison between F_{net} of FOCI and F_{EPR} of MM and LL must, however, be considered carefully since FOCI includes the freezing and melting of sea ice while MM and LL do not.

The most striking difference between the temporal and zonal-mean freshwater fluxes of the different models is the strong meridional variation in FOCI compared to MM and LL (Fig. 11). In general, FOCI has less FWF into the ocean than MM and LL south of 60°S, except for a few peaks like at 66°S (Fig. 11). North of 57°S, FOCI has a stronger FWF into the ocean than the other two models. The stair structure of the FWF in FOCI is due to the large atmosphere-to-ocean ratio of horizontal resolution, 4:1, i.e. ECHAM N48 is four times coarser than NEMO ORCA05, while both LL and MM have nearly a 1:1 ratio of horizontal resolutions. The main difference regarding the zonal and temporal mean FWF between MM and LL is that the one of MM is predominantly stronger south of 65°S and weaker north of it up to 50°S (Fig. 11).

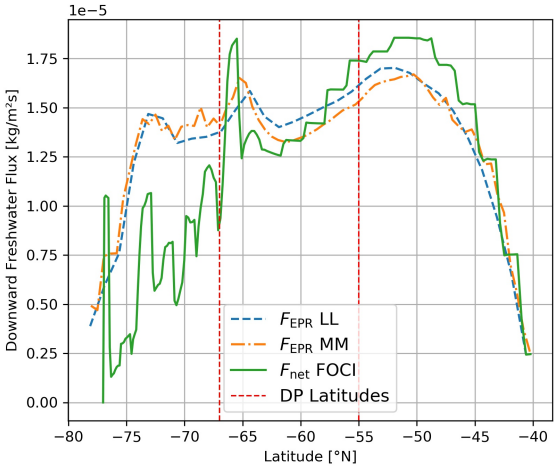

Figure 11: Temporal and zonal mean of F_{net} of FOCI and F_{EPR} of LL and MM. The DP latitude band from section one (see Fig. 1) is indicated by red dashed lines.

The zonal-mean density and salinity profiles in DJF and JJA look quite similar to the temporal mean fields (compare Fig. 10, Fig. 12 and Fig. 13). This is in good agreement with DP transports of the models having no seasonality, since it suggests that the baroclinic part of the ACC driven by meridional density gradients has no annual cycle either.

The freshwater fluxes, however, differ between both seasons and the temporal mean (compare Fig. 11, Fig. 12 and Fig. 13). In general, the FWF is weaker in the north of the SO and stronger in the south for all models in JJA compared to DJF. In LL and MM these differences are mainly caused by different evaporation-precipitation patterns (Fig. 13 and 12). The runoff from rivers and icebergs has a significant influence in DJF south of 64°S.

The main difference between FOCI and the two HadGEM models in both seasons is again the stronger meridional variation of F_{net} of FOCI. Like in the temporal mean, F_{net} of FOCI seems to be lower than F_{EPR} of LL south of 60°S in both seasons. This difference is bigger in JJA. Towards the north, the F_{net} of FOCI is higher than F_{EPR} of MM and LL in both

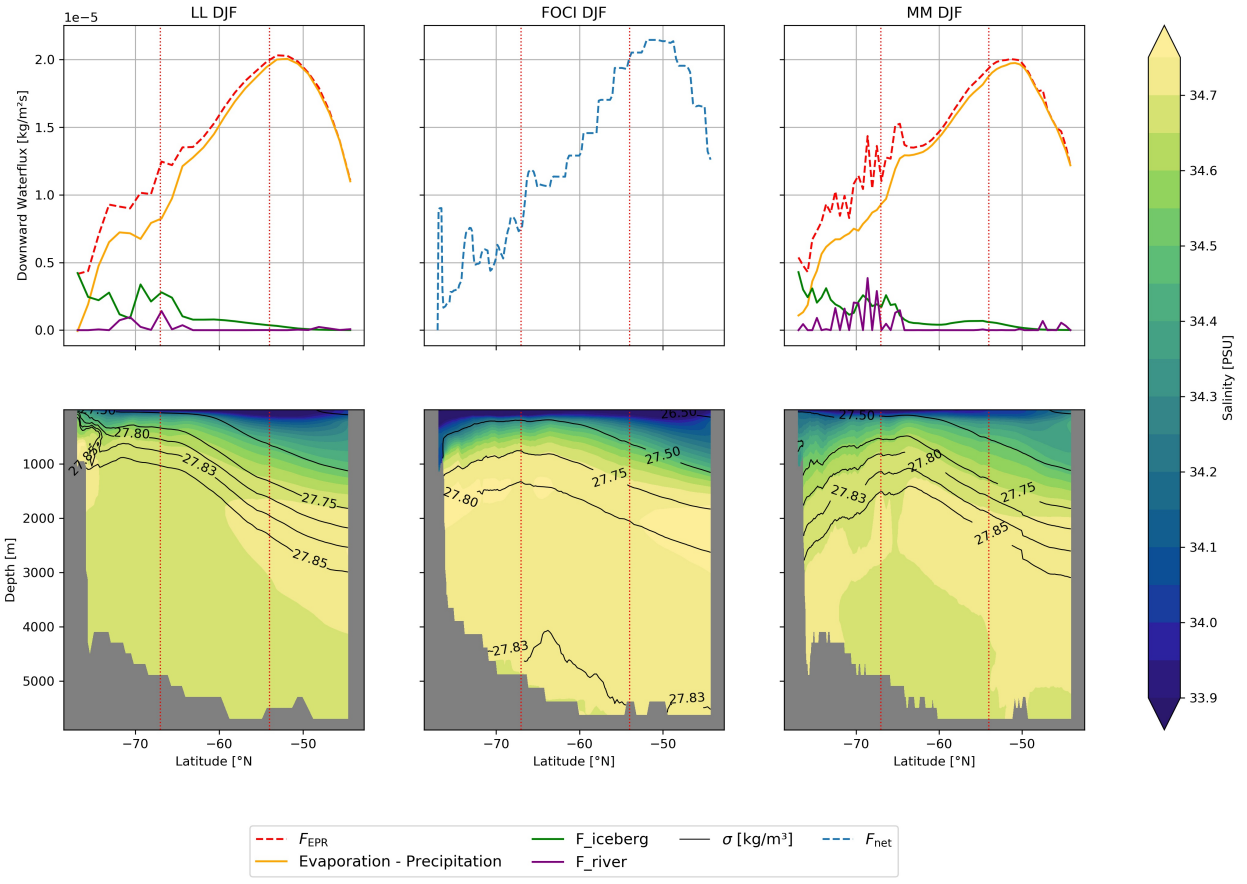

Figure 12: FWF and salinity in the summer season (DJF). Lower row: Zonal mean of the salinity with σ contour lines (black lines). Upper row: Zonal mean of the FWF components and their sum (F_{EPR}) for MM and LL and the F_{net} of FOCI. F_iceberg and F_river are the runoffs from rivers and icebergs. The DP latitude band from section one (see Fig. 1) is indicated by dotted red lines.

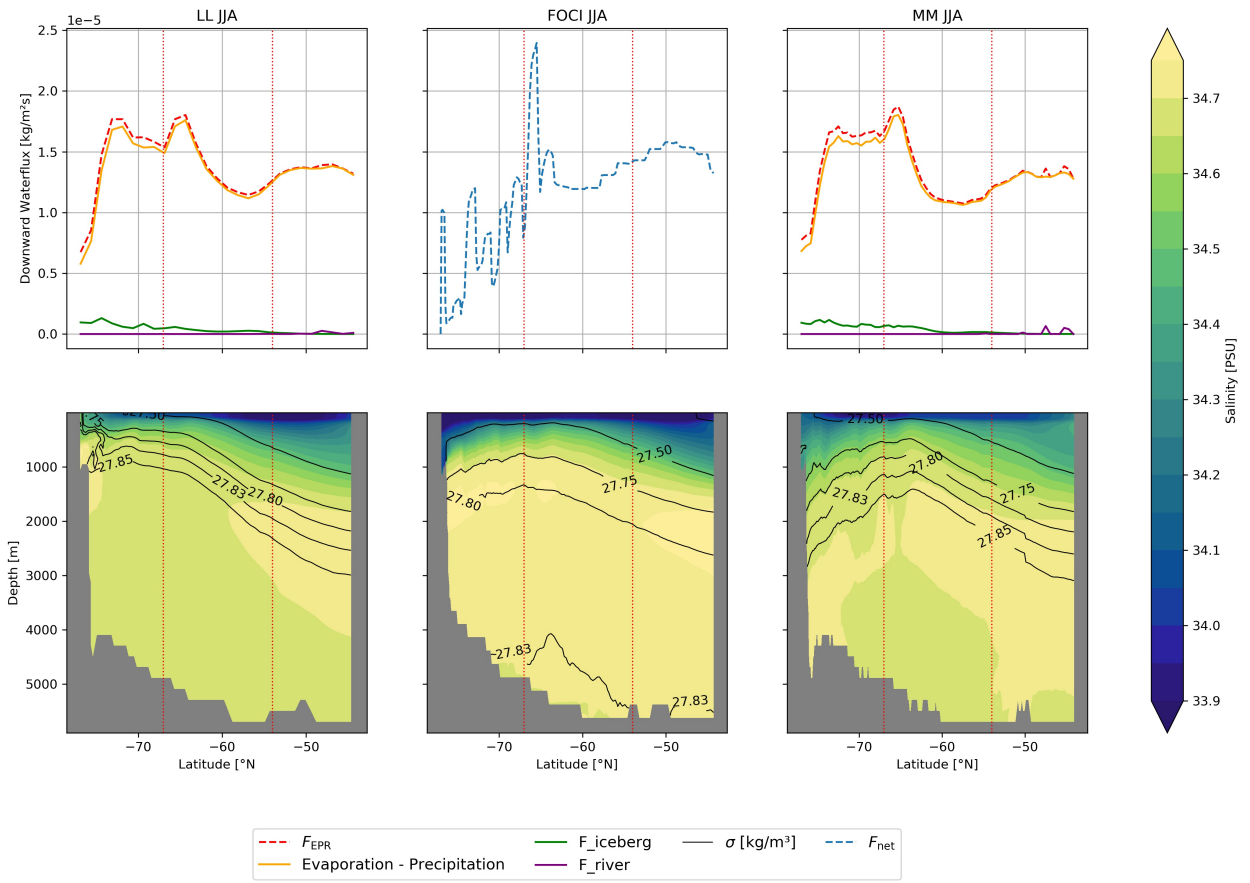

Figure 13: FWF and salinity in the winter season (JJA). Lower row: Zonal mean of the salinity with σ contour lines (black lines). Upper row: Zonal mean of the FWF components and their sum (F_{EPR}) for MM and LL and the F_{net} of FOCI. F_iceberg and F_river are the runoffs from rivers and icebergs. The DP latitude band from section one (see Fig. 1) is indicated by dotted red lines.

seasons.

The MM and LL models differ only slightly in both seasons. The general pattern of the F_{EPR}, with MM being higher than LL at high latitudes and lower towards the north, reoccurs in both seasons. Another difference between MM and LL is the increased smoothness of the river runoff in LL compared to MM, resulting in a more smooth F_{EPR} in DJF (Fig. 12). This is probably due to the smaller grid cells in MM, resulting in more river runoff per unit area. Comparing the runoff from rivers and icebergs in DJF in MM, it is noticeable, that runoff from icebergs is more smooth than from rivers. This is caused by rivers flowing into the nearest grid cell of the ocean, i.e. only ocean grid cells along the coast, while icebergs are advected of the coast, spreading the meltwater over a wider region. The higher horizontal variations of F_{net} in FOCI compared to LL and MM can also be explained this way. The models treat precipitation over land different. In FOCI, JSBACH3 performs river routing and both solid and liquid precipitation is led back to the ocean in rivers, causing a highly

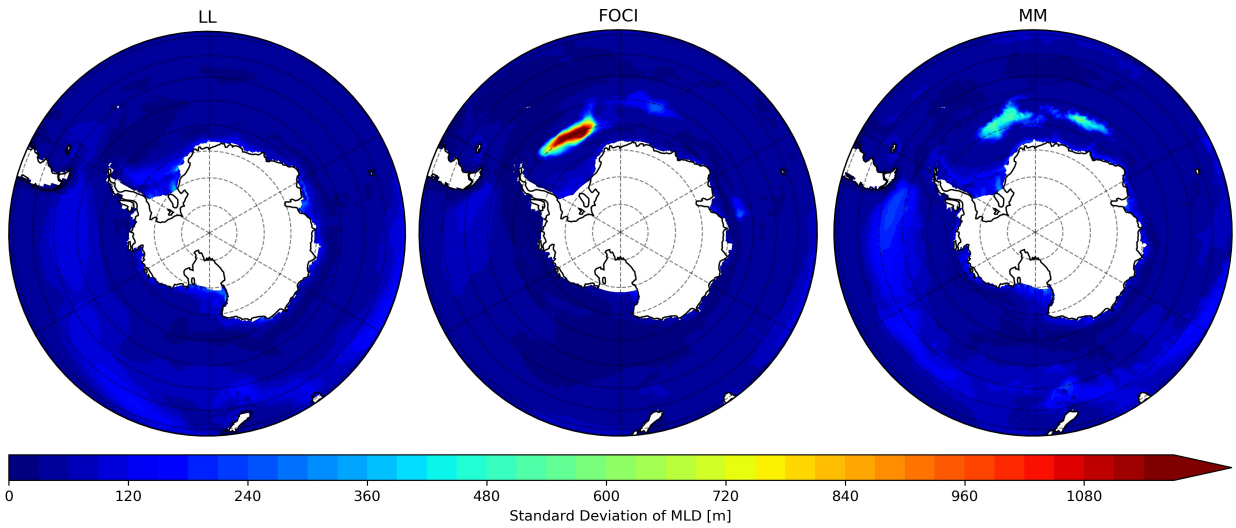

Figure 14: Standard deviation of the MLD

variable F_{net} near the coast. In the HadGEM models, solid precipitation over land becomes part of icebergs, which are advected off the coast and do therefore spread the meltwater over a wider ocean region, which results in smoother zonal-mean F_{EPR}. Additionally, FOCI includes melting and freezing sea ice, which is another possible reason for higher meridional variations of its F_{net}, since sea ice formation happens in certain regions, which would cause a low F_{net} there.

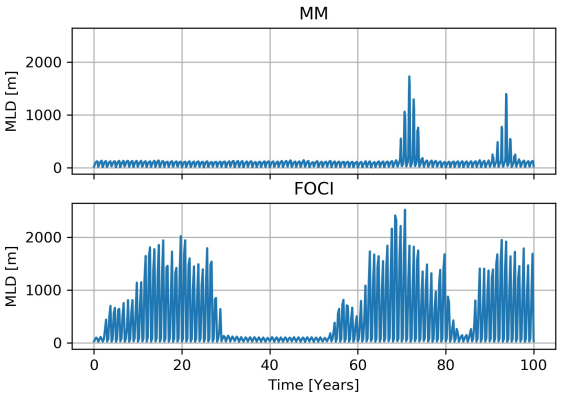

Figure 15: Timeseries of the mean MLD in the areas with deep convection (the exact coordinates of the areas are given in Tab. 3).

To quantify the influence of the different freshwater fluxes south of 63°S where the slumping of the isopycnals and isohalines occurs in the zonal mean density fields (Sec. 3.4), the salinity differences ΔS in a 100 m thick mixed layer caused by F_{EPR} and F_{net} differences (ΔFWF) of the models in the latitude band between 77°S and 63°S, are calculated. The mean downward FWF of this region for each model is given in Tab. 4. From those, ΔFWF between MM and LL or respectively FOCI and LL is calculated, which are also given in Tab. 4, together with the freshwatercolumn Δz that yields from ΔFWF applied over 100 years and the respective salinity difference ΔS caused by adding Δz to the mixed layer.

The calculated ΔS show that the fresher surface water masses south of 63°S in MM compared to LL match with higher freshwater fluxes in MM. On the other hand, FOCI should be saltier than LL based on the freshwater fluxes, which disagrees with FOCI being fresher than LL in the south (Section 3.5).

Another mechanism that could cause the doming of the isopycnals found in MM and FOCI (cf. Fig. 8) is deep convection. The standard deviation of the MLD indicates that deep convection occurs in the Weddell Sea in FOCI and MM (Fig. 14). In LL, no such areas are found. Deep convection is more common in FOCI than in MM. In the Weddell Sea, deep convection happens most of the years in FOCI, while only two events with reoccurring deep convection in five-six consecutive years are observed in MM (Fig. 15). This is also supported by the maximum standard deviation of the MLD of FOCI being more than twice as high as in MM (Fig. 14).

4. Discussion

The low DP transports of 150 Sv, 78 Sv and 80 Sv for LL, FOCI and MM are in good agreement with the transports found by *Roberts et al.* (2019) who stated a transport of 155 Sv and 90 Sv for LL and MM and *Matthes et al.* (2020) who estimated the DP transport of FOCI to be around 83 Sv. The differences are most likely caused by the use of different sections over the DP to calculate the DP transport and different model data. *Roberts et al.* (2019) used the full spinup- and control-1950 runs and *Matthes et al.* (2020) used the full FOCI-piCtl run for the calculation of the mean DP transports.

The only model with DP transport within the observational range of (173.3 ± 10.7) Sv (*Donohue et al.*, 2016) and (133 ± 7) Sv (*Meredith et al.*, 2011) is LL, while MM and FOCI are below. This discrepancy of FOCI and MM is directly linked to the horizontal structure of the ACC. Both MM and FOCI are able to reproduce the complex latitudinal variations of the ACC in the DP, while LL has one broad current. However, the existence of strong westward countercurrents in the temporal mean with zonal velocities of -10 $\mathrm{cm\,s^{-1}}$ and lower like in MM (Fig. 2) is not proven by current observations (*Firing et al.*, 2011; *Chidichimo et al.*, 2014). *Firing et al.* (2011) calculated the time-mean depth integrated transport in the upper 1042 m across section two (their Fig. 4). This can be compared to the time-mean depth integrated transport in the upper 1000 m across section one (Fig. 5), since the zonal velocities of the models do not vary much between section one and two (Fig. 2). It can clearly be seen, that the transport of MM and FOCI is around 0.5 Sv or respectively 1.5 Sv too high in the SAF, while the PF and the SACCF are not represented by both models, having low or sometimes even negative transports south of 58°S, which are more pronounced in MM, due to the stronger countercurrents. The hypothesis that countercurrents lead to the weak DP transport of MM is also supported by *Menary et al.* (2018).

The time-mean zonal wind stress is likely not the cause of the ACC strength biases among the resolution hierarchy since it is nearly equal in MM and LL which is also proven by *Menary et al.* (2018). Additionally, the zonal wind stress has pronounced seasonal variability (Fig. 6) which is not compatible with the DP transports, showing no clear annual cycle (Fig. 4). Furthermore, the DP transport is neither statistically significant related to the latitude of the zonally averaged westerly wind stress maximum nor the total westerly wind stress over the SO among CMIP5 models (*Beadling et al.*, 2019) which also supports our conclusion.

Beadling et al. (2019) used the zonally and full depth-averaged potential density difference $\Delta\rho$ between 65°S and 45°S as a key metric of a realistic representation of ACC in CMIP5 climate models. Compared with their observational estimate of $\Delta\rho = 0.27$ calculated from the World Ocean Atlas 2013 product, all three models of this study with a $\Delta\rho$ of 0.18 $\mathrm{kg\,m^{-3}}$,

$0.16\,\mathrm{kg\,m^{-3}}$ and $0.16\,\mathrm{kg\,m^{-3}}$ for LL, FOCI and MM respectively, are too low in $\Delta\rho$ and would thus be expected to exhibit a weak ACC. The reason for the small differences in $\Delta\rho$ is that the slumping of the isopycnals in FOCI and MM is only observed from 63°S south (Fig. 8). Therefore, $\Delta\rho$ between 65°S and 45°S is only slightly affected by the lower densities in FOCI and MM south of 63°S.

That the meridional density gradient partly explains the difference in DP transports despite the fact $\Delta\rho$ is only different by $0.02\,\mathrm{kg\,m^{-3}}$, is examined in section 3.4. The DP transports calculated from the thermal wind balance are found to have a comparable gradation as the directly modelled transports with LL having the highest DP transport of 69 Sv and FOCI and MM having clearly lower transports of 44 Sv and 36 Sv respectively. The fact that the DP transport calculated from the thermal wind is higher in FOCI than in MM, which is the other way around for the modelled transports, can be explained by the different representation of the countercurrents in the thermal winds. The thermal wind does not show FOCI's countercurrent in the middle of DP, while the countercurrent of MM at the same position is included, but with a more baroclinic structure (Fig. 7). This implies that other drivers of countercurrents must exist causing eastward velocities near the bottom, which is reasonable since the thermal wind only directly includes the Coriolis force, the pressure gradient force and gravity. However, differences between the structure of the thermal winds and the model velocities in the DP also arise from the different latitudes which velocities and scalar quantities are taken at (see Sec. 2.2.2). Differences between modelled transport and thermal wind may also be due to bottom drag or wind stress which are not included in thermal wind calculations. Due to this assumption, the barotropic component of the DP transport is not taken into account, which is an explanation for the transports based on the thermal winds being only around 50% of the total transport. Further investigation of the barotropic component of the ACC among the resolution hierarchy is therefore necessary. In this respect, it would be interesting to examine how the improved ability of higher-resolution models to represent topography impacts the ACC.

Salinity differences explain much of the density gradient differences at high latitudes, supported by the thermal expansion coefficient β_T being one order of magnitude smaller than the haline contraction coefficient β_S near the surface (*Marshall and Plumb*, 2008). On the other hand, β_T increases with depth, while β_S decreases with depth (*Marshall and Plumb*, 2008). Therefore, the influence of temperature on the density grows with depth. The MM model has a warm bias in the SO which reaches over the whole watercolumn, except for the top 1000 m between 80°S and 70°S, where a cold bias predominates (see *Kuhlbrodt et al.* (2018) Fig. 7). Such a cold bias is not present in LL, which coincides with the colder temperatures of MM compared to LL that we found in this area. A warm bias in the SO of

FOCI was also found by *Matthes et al.* (2020). *Kuhlbrodt et al.* (2018) additionally stated that there is a negative salinity bias in MM in the top 1000 m between 80°S and 60°S that they do not observe in LL, which is in agreement with our findings of a fresher ocean in MM compared to LL in the upper 1000 m from 63°S to the southern margin of the SO. However, *Kuhlbrodt et al.* (2018) came to the conclusion that the weak ACC of MM is a consequence of its warm bias in the SO. *Jonathan et al.* (2020) showed that this warm bias is generated by heat uptake at depth in the 30 years long spin-up phase of the model. Such a heat uptake is also considered to happen in FOCI (*Matthes et al.*, 2020). Even though the warm bias of FOCI and MM in the deep SO compared to LL is visible in Fig. 10, we did not further consider it due to the good alignment of the isohalines with the isopycnals. Examining the relation of the SO warm bias found in MM and FOCI to their low DP transports could be an exciting subject for future studies.

Our comparison of the freshwater fluxes must be carefully interpreted, since F_{net} of FOCI includes the effects of sea-ice, whereas F_{EPR} of MM and LL does not. Sea-ice is generally formed near the Antarctic coast and subsequently advected to the north where it melts. Therefore, including sea ice in the FWF leads to lower values at high latitudes and higher values at low latitudes, which is exactly how FOCI differs from MM and LL (Fig. 11). This hypothesis is also supported by bigger differences between FOCI's low F_{net} and the higher F_{EPR} of MM and LL south of 60°S in JJA, the main season of sea ice formation.

Calculating the expected mixed-layer salinity differences between LL, MM and FOCI from the freshwater fluxes, we expect FOCI to be $\Delta S = 5.423$ PSU saltier than LL south of 63°S. Since FOCI is actually found to be fresher than LL, the positive ΔS is considered to be an artefact of neglecting sea ice in the FWF of LL. The stronger freshwater fluxes in MM compared to LL would on the one hand cause the mixed layer to be 0.605 PSU fresher than in LL. On the other hand, this difference seems to be small, considering the strong constraints of a 100m deep mixed layer and the exclusion of advection or mixing that we make in this estimate. The question of how sea ice is connected to the DP transport is an interesting issue that could be pursued in the future. The warm bias in the SO of FOCI and MM leads to a negative sea ice bias with sea ice extents of the FOCI's historical setup being up to five times smaller in September than the observational estimates (*Matthes et al.*, 2020). The sea ice extents of MM are comparable to FOCI (*Menary et al.*, 2018). The meltwater from the sea ice probably freshens the SO, which could be another explanation for the fresher oceans near the surface in MM and FOCI compared to LL, which has no distinctive sea ice bias (*Williams et al.*, 2018).

Another aspect that needs to be discussed is deep convection in Weddell Sea in MM and

FOCI. We find reoccurring deep convection in the Weddell Sea for FOCI, which is consistent with the results of *Matthes et al.* (2020). Nevertheless, only two events of deep convection in the Weddell Sea were found in MM, which contradicts *Menary et al.* (2018), who suggested permanent deep convection in this region in MM. A possible reason for this contradiction is that they use a 300-year time series of the pre-industrial control run with constant forcing appropriate for the year 1850, whereas we only use a 100-year time series of the control-1950 run with constant forcing of the year 1950. The fact that there is no deep convection in LL is also confirmed by *Menary et al.* (2018).

Due to the different horizontal resolutions of the models, the values of parameters for diffusion, time step etc. vary. Higher-resolution models typically have less strong isopycnal diffusion (e.g. Tab. 2 in *Roberts et al.* (2019)) and viscosity. This means, that stronger shear is permitted in higher-resolution models, which is a likely explanation for the more pronounced horizontal variability of the ACC in MM and FOCI (Fig. 3). Differences in the parameterisation of mesoscale eddies could result in different simulated DP transports (*Kuhlbrodt et al.*, 2012). However, if the parameterisation would be the cause for the ACC strength biases, FOCI and LL should be similar because both use eddy parameterisation, while MM uses no parameterisation for mesoscale eddies. Since this is not the case, eddy parameterisation is eliminated as a reason for the ACC strength biases of the models.

5. Summary and Conclusion

We find significantly lower time-mean DP transports of 78 Sv for FOCI with a 1/2° ocean model and 80 Sv for MM with a 1/4° ocean model than for LL with 150 Sv and a 1° ocean model, agreeing with current observations of the DP transport. The biases of ACC strength in the high resolution ocean models are found to be directly linked to a more pronounced horizontal structure of the ACC with too low zonal velocities in the DP south of 58°S. In the middle of the DP and near its southern margin, westward countercurrents are observed which are stronger in MM with zonal velocities down to to -23 $\mathrm{cm\,s^{-1}}$. This is not consistent with current ACC observations. The low DP transport south of 58°S in FOCI and MM is partly compensated by eastward northern boundary currents with velocities higher than observational values.

As two possible drivers of the ACC that could account for the model biases in ACC strength, the zonal wind stress and the meridional density gradient are considered. Since the zonal wind stress is nearly equal in MM and LL which, in turn, are comparable to FOCI, zonal wind stress is not considered to account for the biases in DP transport. The meridional density gradient, however, is identified as a leading order driver of the ACC which explains part of the transport differences between the models. This is due to the fact, that the volume transport caused by the density gradient trough the DP is found to be 46%, 45% and 58% of the total transport of LL, FOCI and MM respectively, by using the thermal wind equation (Eg. 3). Furthermore, the velocity structure from the thermal wind balance is found to be comparable to the one of the directly modelled velocities.

The same methodology applied to the zonal mean meridional density gradient yields transports through DP of 79 Sv, 40 Sv and 49 Sv for LL, FOCI and MM respectively. The lower values of FOCI and MM are again found to be based on countercurrents, this time reaching from the southern margin of the SO to 63°S. Hence positive or low meridional density gradients due to too low densities in the south cause a weak ACC not only in DP but everywhere around the Antarctic Continent.

It is still not fully understood how this density bias in FOCI and MM is precisely set. Lower densities of FOCI and MM south of 63°S are found to be linked to fresher upper oceans in this region compared to LL. The negative salinity bias in MM can be partly explained by higher FWFes south of 63°S. In FOCI, reoccurring deep convection in the Weddell Sea is observed, which leads to a flattening of the isopycnals over the whole watercolumn (*Menary et al.*, 2018). Another possible reason for the low densities we found in MM and FOCI is their warm bias in the SO. It must also be considered, that the baroclinic transport derived from the meridional density gradient is only approx. 50% of the models DP transport. Additional

investigation on how the density bias in FOCI and MM is set and which role the barotropic ACC component plays in setting the ACC strength bias is therefore needed.

6. References

Beadling, R. L., J. L. Russell, R. J. Stouffer, P. J. Goodman, and M. Mazloff (2019), Assessing the quality of Southern Ocean circulation in CMIP5 AOGCM and earth system model simulations, *Journal of Climate*, *32*(18), 5915–5940, doi:10.1175/JCLI-D-19-0263.1.

Brovkin, V., T. Raddatz, C. H. Reick, M. Claussen, and V. Gayler (2009), Global biogeophysical interactions between forest and climate, *Geophysical Research Letters*, *36*(7), 1–5, doi:10.1029/2009GL037543.

Chidichimo, M. P., K. A. Donohue, D. R. Watts, and K. L. Tracey (2014), Baroclinic transport time series of the Antarctic Circumpolar Current measured in Drake Passage, *Journal of Physical Oceanography*, *44*(7), 1829–1853, doi:10.1175/JPO-D-13-071.1.

Donohue, K. A., K. L. Tracey, D. R. Watts, M. P. Chidichimo, and T. K. Chereskin (2016), Mean Antarctic Circumpolar Current transport measured in Drake Passage, *Geophysical Research Letters*, *43*(22), 11,760–11,767, doi:10.1002/2016GL070319.

Fichefet, T., and M. A. Maqueda (1997), Sensitivity of a global sea ice model to the treatment of ice thermodynamics and dynamics, *Journal of Geophysical Research: Oceans*, *102*(C6), 12,609–12,646, doi:10.1029/97JC00480.

Firing, Y. L., T. K. Chereskin, and M. R. Mazloff (2011), Vertical structure and transport of the Antarctic Circumpolar Current in Drake Passage from direct velocity observations, *Journal of Geophysical Research: Oceans*, *116*(8), 1–16, doi:10.1029/2011JC006999.

Gent, P. R., and J. C. Mcwilliams (1990), Isopycnal Mixing in Ocean Circulation Models, *Journal of Physical Oceanography*, *20*(1), 150–155, doi:10.1175/1520-0485(1990)020⟨0150:IMIOCM⟩2.0.CO;2.

Gill, A. E. (1982), *Atmosphere-Ocean Dynamics*, 662 pp., Academic Press, San Diego, MA.

Haarsma, R. J., et al. (2016), High resolution model intercomparison project (highresmip v1.0) for cmip6, *Geoscientific Model Development*, *9*(11), 4185–4208, doi:10.5194/gmd-9-4185-2016.

Hunke, E. C., W. H. Lipscomb, A. K. Turner, N. Jeffery, and S. Elliot (2015), *CICE: the Los Alamos sea ice model documentation and software user's manual Version 5.1*, Los Alamos, NM.

Jackett, D. R., and T. J. Mcdougall (1995), Minimal Adjustment of Hydrographic Profiles to

Achieve Static Stability, *Journal of Atmospheric and Oceanic Technology*, *12*(2), 381–389, doi:10.1175/1520-0426(1995)012⟨0381:MAOHPT⟩2.0.CO;2.

Jonathan, T., H. Johnson, D. Marshall, M. Bell, and P. Hyder (2020), Antarctic Circumpolar Current Biases in a hierarchy of HadGEM3-GC3.1 Models, *EGU General Assembly 2020, Online, 4–8 May 2020, EGU2020-11444*, doi:https://doi.org/10.5194/egusphere-egu2020-11444.

Kjellsson, J., P. R. Holland, G. J. Marshall, P. Mathiot, Y. Aksenov, A. C. Coward, S. Bacon, A. P. Megann, and J. Ridley (2015), Model sensitivity of the Weddell and Ross seas, Antarctica, to vertical mixing and freshwater forcing, *Ocean Modelling*, *94*(November), 141–152, doi:10.1016/j.ocemod.2015.08.003.

Kuhlbrodt, T., R. S. Smith, Z. Wang, and J. M. Gregory (2012), The influence of eddy parameterizations on the transport of the Antarctic Circumpolar Current in coupled climate models, *Ocean Modelling*, *52-53*, 1–8, doi:10.1016/j.ocemod.2012.04.006.

Kuhlbrodt, T., et al. (2018), The Low-Resolution Version of HadGEM3 GC3.1: Development and Evaluation for Global Climate, *Journal of Advances in Modeling Earth Systems*, *10*(11), 2865–2888, doi:10.1029/2018MS001370.

Lumpkin, R., and K. Speer (2007), Global ocean meridional overturning, *Journal of Physical Oceanography*, *37*(10), 2550–2562, doi:10.1175/JPO3130.1.

Madec, G., et al. (2017), Nemo ocean engine, doi:10.5281/zenodo.1472492.

Marshall, J., and R. A. Plumb (2008), *Atmosphere, Ocean and Climate Dynamics: An Introductory Text*, Elsevier Academic Press, San Diego, CA.

Matthes, K., et al. (2020), The Flexible Ocean and Climate Infrastructure Version 1 (FOCI1): Mean State and Variability, *Geoscientific Model Development Discussions*, *1*(January), 1–53, doi:10.5194/gmd-2019-306.

Mazloff, M. R., P. Heimbach, and C. Wunsch (2010), An eddy-permitting Southern Ocean state estimate, *Journal of Physical Oceanography*, *40*(5), 880–899, doi:10.1175/2009JPO4236.1.

Meijers, A. (2014), The southern ocean in the coupled model intercomparison project phase 5, *Philosophical transactions. Series A, Mathematical, physical, and engineering sciences*, *372*, doi:10.1098/rsta.2013.0296.

Menary, M. B., et al. (2018), Preindustrial Control Simulations With HadGEM3-GC3.1

for CMIP6, *Journal of Advances in Modeling Earth Systems*, *10*(12), 3049–3075, doi: 10.1029/2018MS001495.

Meredith, M. P., et al. (2011), Sustained monitoring of the Southern Ocean at Drake Passage: Past achievements and future priorities, *Reviews of Geophysics*, *49*(4), 1–36, doi:10.1029/2010RG000348.

Olbers, D., J. Willebrand, and C. Eden (2012), *Ocean Dynamics*, Springer, Berlin, GER, doi:10.1007/978-3-642-23450-7.

Orsi, A. H., T. Whitworth, and W. D. Nowlin (1995), On the meridional extent and fronts of the Antarctic Circumpolar Current, *Deep-Sea Research Part I*, *42*(5), 641–673, doi: 10.1016/0967-0637(95)00021-W.

Orsi, A. H., G. C. Johnson, and J. L. Bullister (1999), Circulation, mixing, and production of Antarctic Bottom Water, *Progress in Oceanography*, *43*(1), 55–109, doi: 10.1016/S0079-6611(99)00004-X.

Reid, J. L. (1997), On the total geostrophic circulation of the pacific ocean: flow patterns, tracers, and transports, *Progress in Oceanography*, *39*(4), 263 – 352, doi:https://doi.org/10.1016/S0079-6611(97)00012-8.

Rintoul, S. R., C. W. Hughes, and D. Olbers (2001), Chapter 4.6 the antarctic circumpolar current system, in *Ocean Circulation and Climate*, *International Geophysics*, vol. 77, edited by G. Siedler, J. Church, and J. Gould, pp. 271 – 302, Academic Press, San Diego, CA, doi:https://doi.org/10.1016/S0074-6142(01)80124-8.

Roberts, M. J., et al. (2019), Description of the resolution hierarchy of the global coupled HadGEM3-GC3.1 model as used in CMIP6 HighResMIP experiments, *Geoscientific Model Development*, *12*(12), 4999–5028, doi:10.5194/gmd-12-4999-2019.

Russell, J. L., R. J. Stouffer, and K. W. Dixon (2006), Intercomparison of the Southern Ocean circulations in IPCC coupled model control simulations, *Journal of Climate*, *19*(18), 4560–4575, doi:10.1175/JCLI3869.1.

Stevens, B., et al. (2013), Atmospheric component of the MPI-M earth system model: ECHAM6, *Journal of Advances in Modeling Earth Systems*, *5*(2), 146–172, doi:10.1002/jame.20015.

Talley, L. D., G. L. Pickard, W. J. Emery, and J. H. Swift (2011), Chapter 13 - southern ocean, in *Descriptive Physical Oceanography (Sixth Edition)*, edited by L. D. Talley, G. L.

Pickard, W. J. Emery, and J. H. Swift, sixth edition ed., pp. 437 – 471, Academic Press, San Diego, CA, doi:https://doi.org/10.1016/B978-0-7506-4552-2.10013-7.

Tansley, C. E., and D. P. Marshall (2001), On the dynamics of wind-driven circumpolar currents, *Journal of Physical Oceanography*, *31*(11), 3258–3273, doi:10.1175/1520-0485(2001)031⟨3258:OTDOWD⟩2.0.CO;2.

Treguier, A. M., I. M. Held, and V. D. Larichev (1997), Parameterization of Quasigeostrophic Eddies in Primitive Equation Ocean Models, *Journal of Physical Oceanography*, *27*(4), 567–580, doi:10.1175/1520-0485(1997)027⟨0567:POQEIP⟩2.0.CO;2.

Valcke, S. (2013), The OASIS3 coupler: a European climate modelling community software, *Geoscientific Model Development*, *6*(2), 373–388, doi:10.5194/gmd-6-373-2013.

Vallis, G. (2006), *Atmospheric and Oceanic Fluid Dynamics*, 745 pp., Cambridge University Press, Cambridge, UK, doi:10.2277/0521849691.

Walters, D., et al. (2019), The Met Office Unified Model Global Atmosphere 7.0/7.1 and JULES Global Land 7.0 configurations, *Geoscientific Model Development*, *12*(5), 1909–1963, doi:10.5194/gmd-12-1909-2019.

Watterson, I. G., J. Bathols, and C. Heady (2014), What influences the skill of climate models over the continents?, *Bulletin of the American Meteorological Society*, *95*(5), 689–700, doi:10.1175/BAMS-D-12-00136.1.

Williams, K. D., et al. (2018), The Met Office Global Coupled Model 3.0 and 3.1 (GC3.0 and GC3.1) Configurations, *Journal of Advances in Modeling Earth Systems*, *10*(2), 357–380, doi:10.1002/2017MS001115.

Appendix

Derivation of Ekman Dynamics

The complete three dimensional momentum equation can be written as (cf. *Gill* (1982)):

$$\boxed{\frac{D\vec{u}}{Dt} = \frac{\partial \vec{u}}{\partial t} + (\vec{u}\cdot\nabla)\vec{u} = -\frac{1}{\rho}\nabla p - \nabla\Phi^E - \vec{f}\times\vec{u} + \nabla_h^2\vec{u}A_h + \frac{\partial^2\vec{u}}{\partial z^2}A_v,} \tag{4}$$

where $\vec{u}$ is the velocity, ρ density, p pressure, Φ^E geopotential, $\vec{f}$ the coriolis parameter, A_h the horizontal friction parameter and A_v the vertical friction parameter.

The advectional terms $(\vec{u}\cdot\nabla)\vec{u}$ in Eq. 4 can be neglected because of the Rossby number R_0 being far smaller than one (*Gill*, 1982). Horizontal friction can also be neglected in the frictional layer of the ocean, since the main stress acts in horizontal direction (wind stress, bottom friction) and variations of it are much smaller in horizontal than in vertical direction. The frictional terms can therefore be written as $\frac{\partial^2\vec{u}}{\partial z^2}A_v = \frac{\partial}{\partial z}\vec{\tau}$ with $\vec{\tau}$ being the inter layer stress. If furthermore the assumption is made, that $\nabla\Phi^E$ has only a vertical component, the horizontal momentum equation can be written as (cf. *Gill* (1982)):

$$\frac{\partial\vec{u}}{\partial t} = -\vec{f}\times\vec{u} - \frac{1}{\rho}\nabla p + \frac{\partial}{\partial z}\vec{\tau}. \tag{5}$$

By separating the geostrophic velocity $\vec{u_g}$ and ageostrophic velocity $\vec{u_{\mathrm{ag}}}$ with $\vec{u} = \vec{u_g} + \vec{u_{\mathrm{ag}}}$, Eq. 5 can be split into a geostrophic and an ageostrophic part (cf. *Gill* (1982)). Additionally, a stationary state is assumed ($\frac{\partial\vec{u}}{\partial t} = 0$)

$$\begin{aligned} \vec{f}\times\vec{u_g} &= -\frac{1}{\rho}\nabla p, \\ \vec{f}\times\vec{u_{\mathrm{ag}}} &= \frac{\partial}{\partial z}\vec{\tau}. \end{aligned} \tag{6}$$

The velocity u_{ag} is also referred to as the Ekman velocity u_E. The unit less Ekman number (E_k) is used to determine the importance of vertical friction

$$E_k = \mathcal{O}\left(\frac{\text{Friction}}{\text{Coriolis}}\right) = \frac{A_v\frac{U}{H^2}}{fU} = \frac{A_v}{fH^2}.$$

H_E is defined as the depth until which friction plays a role ($E_k = 1$):

$$E_k = 1 = \frac{A_v}{f H_E^2}$$
$$H_E = \sqrt{\frac{A_v}{f}}$$

To obtain the Ekman transport in the ocean-atmosphere frictional layer (M_E) caused by u_E, the vertical integral from H_E to the surface of u_E is calculated (cf. *Gill* (1982)):

$$\vec{M_E} = \int_{H_E}^{0} u_E dz \tag{7}$$

Together with Eq. 6, Eq. 7 yields:

$$\vec{f} \times \vec{u_E} = \frac{\partial \tau}{\partial z} \quad \left| \int_{H_E}^{0} dz \right.$$
$$\vec{f} \times \vec{M_E} = \vec{\tau}|_{z=0} - \vec{\tau}|_{z=H_E} .$$

With τ = wind stress (τ_{wind}) at $z = 0$ and $\tau = 0$ at $z = H_E$, Eq. 1 is obtained (cf. *Gill* (1982)). The convergence of M_E then sets the the Ekman suction/pumping w_E (Eq. 2).

Derivation of the Thermal Wind Equations

Neglecting the material derivate of the velocity in Eq. 4 can be shown as reasonable carrying out a scale analysis. By comparing the scales of the advectional term and the time derivate with the coriolis force, the Rossby numbers are obtained:

$$R_0 = \mathcal{O}\left(\frac{\text{Advection}}{\text{Coriolis}}\right) = \frac{U^2}{LfU} = \frac{U}{Lf},$$
$$R_{0_T} = \mathcal{O}\left(\frac{\text{Time derivate}}{\text{Coriolis}}\right) = \frac{U}{TfU} = \frac{1}{Tf},$$

with R_0 being the spatial Rossby number, R_{0_T} the temporal Rossby number, T order of magnitude of time, and the other upper case letters orders of magnitude of their lower case equivalents. *Vallis* (2006) used characteristic numbers for the large scale flow and showed that both numbers are much smaller than one. He also showed by a scale analysis, that hydrostatic balance holds for the large scale flow. As long as the motion does not happen in frictional boundary layers, the frictional term can also be neglected, which leads to the

geostrophic equations (cf. *Vallis* (2006)

$$fu = -\frac{1}{\rho_0}\frac{\partial p}{\partial y}, \tag{8}$$

$$fv = \frac{1}{\rho_0}\frac{\partial p}{\partial x}, \tag{9}$$

$$g\rho = -\frac{\partial p}{\partial z}, \tag{10}$$

where u is zonal velocity, v meridional velocity and ρ_0 a constant density. It must be noted, that Boussinesq approximation is also used in these equations, which means, that only vertical changes of density are considered (*Gill*, 1982). By cross-differentiating Eq. 8 and 9 with Eq. 10 and then replacing the pressure terms in 8 and 9 with the one in 10, the thermal wind balance (Eq. 3) is obtained (cf. *Vallis* (2006)).

Eidesstattliche Erklärung

Hiermit erkläre ich, dass ich die vorliegende Arbeit selbständig und ohne fremde Hilfe angefertigt und keine anderen als die angegebenen Quellen und Hilfsmittel verwendet habe. Die eingereichte schriftliche Fassung der Arbeit entspricht der auf dem elektronischen Speichermedium. Weiterhin versichere ich, dass diese Arbeit noch nicht als Abschlussarbeit an anderer Stelle vorgelegen hat.

Datum: _____ Unterschrift: _____